Chapter 2
Synchrotron-Radiation-Based Energy-Domain Mössbauer Spectroscopy, Nuclear Resonant Inelastic Scattering, and Quasielastic Scattering Using Mössbauer Gamma Rays

Makoto Seto, Ryo Masuda, and Makina Saito

Abstract Nuclear resonant scattering spectroscopy using synchrotron radiation (SR) has been applied to a wide variety of scientific applications. An excellent feature of this method is that element (isotope)-specific information on the electronic and phonon states can be obtained using the energy selectivity of SR. The use of high-brilliance SR as an excitation source for Mössbauer spectroscopy allows imaging measurement under extreme conditions, such as high pressures, very high or low temperatures, and strong external magnetic fields. Additionally, diffusion and fluctuation of atoms can be observed by taking advantage of the ultranarrow width of the nuclear excited states. We introduced the concepts of the methods with an emphasis on these excellent features. Furthermore, the unique features involved in the measurements are highlighted and discussed.

List of Abbreviations and Symbols

SR	Synchrotron radiation
NRIS	Nuclear resonant inelastic scattering
NIS	Nuclear inelastic scattering
NRIXS	Nuclear resonant inelastic X-ray scattering
NRVS	Nuclear resonant vibrational spectroscopy
PDOS	Phonon density of states
DFT	Density functional theory
RSMR	Rayleigh scattering of Mössbauer radiation
TDI	Time-domain interferometry
APD	Avalanche photo diode
NFS	Nuclear (resonant) forward scattering

M. Seto (✉) · R. Masuda · M. Saito
Institute for Integrated Radiation and Nuclear Science, Kyoto University, Kumatori-Cho,
Sennan-Gun, Osaka 590-0494, Japan
e-mail: seto@rri.kyoto-u.ac.jp

Y. Yoshida and G. Langouche (eds.), *Modern Mössbauer Spectroscopy*,
Topics in Applied Physics 137, https://doi.org/10.1007/978-981-15-9422-9_2

SMS	Synchrotron Mössbauer source
RI	Radioisotope
FWHM	Full width at half maximum
DAC	Diamond anvil cell
QEGS	Quasielastic γ-ray scattering
RC	Radiative coupling

2.1 Introduction

The use of nuclear probes is advantageous for the study of condensed matter because it enables measurement that would be difficult with electron systems; it gives isotope-specific information for complex compounds. It is possible to attain atomic position resolution if nuclear probes are implanted at specific positions with atomic resolution such as a special isotope monolayer in an artificial multilayer film made by molecular beam epitaxy method. The hyperfine interactions between nuclei and electrons are useful for information on the electronic states. Mössbauer spectroscopy, which uses the recoilless nuclear resonant absorption effect known as the "Mössbauer effect," is a famous and effective method for the electronic state measurement using the hyperfine interactions [1]. Mössbauer spectroscopy is a powerful and well-established method used in a wide variety of research areas, such as materials, chemical, biological, earth, and fundamental physical sciences. The recoilless fraction gives lattice dynamics information in addition to electronic state information. Since nuclear probes are element (isotope)-specific, measurement with very dilute probes is sometimes possible. Besides, they may even attain atomic layer resolution. Moreover, states of the specific atoms of interest in complex compounds can be elucidated. Another outstanding feature to be addressed is the narrow width of a nuclear excited state compared with the resonant excitation energy (e.g., the width of the first nuclear excited state of ^{57}Fe is 4.66 neV, while the resonant excitation energy is 14.4 keV). This feature can be used for the slow dynamics study of resonant atoms in macromolecules, viscous liquids, etc., by observing the broadening of Mössbauer spectra. With this feature, we can use ultranarrow-width γ-rays as spectroscopic probes for the slow dynamics study of the sample containing no resonant atoms. This method is known as "Rayleigh scattering of Mössbauer radiation (RSMR)" [2].

Radioisotope (RI) sources are used in performing Mössbauer spectroscopy, and the preparation of an RI source for each nuclide to be studied is required. In particular, the measurement laboratory should be placed near to a reactor or an accelerator that generates the RI sources with short lives. Mössbauer effect measurement without preparing the RI sources was achieved using energy-tunable SR as a nuclear excitation source [3]. This achievement made Mössbauer measurement easily accessible for nuclides other than the limited ones (such as ^{57}Fe, ^{119}Sn, and ^{151}Eu) with long-lifetime parent RI sources. However, the photon energy range depends on the storage ring and insertion devices installed (the maximum energy with enough intensity is usually limited to below 10^5 eV). The energy selectivity of SR allows the measurement of ^{40}K Mössbauer spectra, of which the observation is impossible using ordinary radioactive sources because the first excited state of ^{40}K is not populated by any radioactive parent nuclides [4]. Additionally, a prominent advantage of Mössbauer spectroscopy using the energy-tunable SR is the measurement of element (isotope)-specific phonon energy spectra, which is difficult with RI sources [5]. Furthermore, the combination of electronic and phonon-state measurements generates site-specific phonon energy spectra [6]. Moreover, high-brilliance SR enables imaging measurement, high-pressure measurement, the measurement of tiny samples, etc. In particular, this is advantageous for RSMR measurement, which can measure angle-dependent energy transfer and, therefore, requires small angular divergence of the probe γ-rays.

As shown, the use of nuclear excitation process and SR has realized unique and effective spectroscopic methods applicable to vast research areas. Note that nuclear resonant scattering spectroscopy using SR has two aspects. One is that it enables the element (isotope)-specific measurement of electronic states and dynamics with advanced features. The other is the ultranarrow width of the emitted γ-rays. In Sect. 2.2, as an element (isotope)-specific method for electronic state (and slow dynamics) measurement, we discuss synchrotron-radiation-based Mössbauer spectroscopy that yields absorption-type Mössbauer spectra [7]. This method enables advanced measurement using the excellent features of SR, such as Mössbauer spectroscopic measurement under high pressures. Furthermore, this method gives absorption-type spectra similar to those obtained by Mössbauer spectroscopy with RI sources. Since this method was developed in 2009 and the efficiency was much improved recently [8], we explain the details of this method precisely based on some recent results obtained using this method, including the comparison of the other similar methods. In Sect. 2.3, we discuss the nuclear resonant inelastic scattering (NRIS) spectroscopy that gives element (isotope)- and site-specific phonon densities of states. This method is sometimes called "nuclear inelastic scattering (NIS)," "nuclear resonant inelastic X-ray scattering (NRIXS)," and "nuclear resonant vibrational spectroscopy (NRVS)," depending on the scientific field. This method has been very actively applied to research areas, such as condensed matter physics, earth sciences, and biosciences. Recently, the local structure of active sites in enzymes has been studied, and these results are introduced. Moreover, site-specific phonon measurement is explained in addition to element (isotope)-specific phonon measurement. In Sect. 2.4, RSMR using SR is introduced, which uses the ultranarrow width of the emitted γ-rays with high directivity. As discussed, ultranarrow-width γ-rays are produced with this method. It means this method uses only a small part (approximately 10^{-9} eV) out of the much wider width (approximately in the electron volt range) of the SR. Even though the small angular divergence of SR is efficient for the angle-dependent measurement compared with RI sources that emit γ-rays in all directions, much improvement in the efficacy is possible. We recently achieved improvement by developing multiline methods and obtained new results on slow dynamics. The newly developed method is precisely explained, and recent results obtained using this method are introduced.

2.2 Synchrotron Radiation-Based Mössbauer Spectroscopy

SR-based Mössbauer absorption spectroscopy is a method to obtain the Mössbauer energy absorption spectra of various nuclides. As you can see, for instance, in many other chapters in this book, Mössbauer spectroscopy is mostly performed with ^{57}Fe as its isotope probe. However, Mössbauer spectroscopy is also possible with many isotopes other than ^{57}Fe. Mössbauer experiments with these isotopes have been performed using RI even before the development of methods using SR. This situation can be shown in the periodic table of Mössbauer elements, as shown in Fig. 2.1. This table and further information are also shown in the Mössbauer Effect Data Center website [9]. Nevertheless, Mössbauer experiments with isotopes other than ^{57}Fe and ^{119}Sn are by far fewer than those with the two isotopes. One major difficulty is in the preparation of parent nuclides. The γ-ray sources for ^{57}Fe and ^{119}Sn can be purchased, but not for the other nuclides. Hence, nuclear reactors or particle accelerators are required. Some isotopes, for example ^{40}K, have no appropriate parent RI; Mössbauer spectroscopy using this isotope has been performed using the "in-beam" method, where the Mössbauer experimental instruments (often including the cryostat for cooling) have been combined with particle beam irradiation system [10]. This problem is fairly solved if SR is applied as the source. SR-based Mössbauer spectroscopy is one of such methods. In this section, its property, measurement system, and analysis method are described.

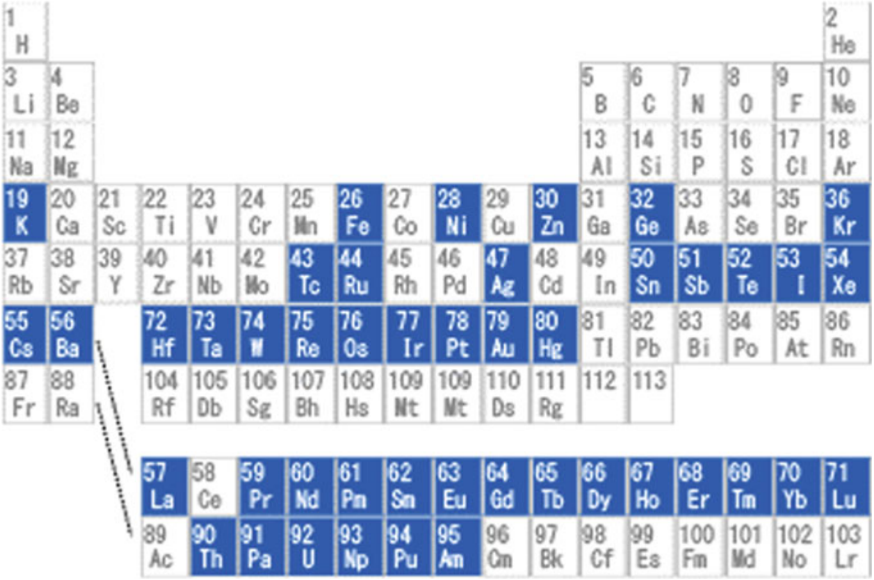

Fig. 2.1 Periodic table of elements in which Mössbauer effect has been observed (reproduced from Seto (2013) [11]

2.2.1 *Special Features*

This method was originally proposed in 1974 [12] and thus is the oldest method of Mössbauer spectroscopy using SR. However, it was developed in 2009 [7] after the development of other methods, such as the synchrotron Mössbauer source (SMS) [13] and nuclear forward scattering (NFS) [14]. The comparison of these methods is mentioned in a later section. Here, we focus on the properties of SR-based Mössbauer spectroscopy. First, as already described, this method is suitable for Mössbauer measurement using various isotopes, especially those with a relatively short half-life of a few nanoseconds. As shown in Fig. 2.2, many isotopes show their half-life in this range. Although iron and tin are present in various materials, new diverse frontier materials are also composed of many elements. Hence, Mössbauer spectroscopy with these isotopes plays a critical role in elucidating the electronic states of their composition elements. For example, isotope selectivity has yielded unique information on samples in monoatomic position resolution in ^{57}Fe Mössbauer spectroscopy [15]. This property has become more important to understand the mechanism of the novel function of frontier materials if it is applied to various resonant isotopes. Until now, SR-based Mössbauer spectroscopy of ^{40}K [17], ^{61}Ni [18], ^{73}Ge [7], ^{119}Sn [19], ^{125}Te [20], ^{127}I, ^{149}Sm [21], ^{151}Eu [22], ^{174}Yb [8], and ^{189}Os [23] has already been performed. This multi-isotope property is due to the whiteness of SR in the energy domain and the measurement mechanism of this method, described in the following section. Second, this method is suitable for tiny sample amounts, often seen in the frontier materials, such as nanoparticles and thin films, and materials under extreme conditions, such as low temperature, high pressure, and gas environment for an in situ experiment, which is due to the high brilliance of SR. Third,

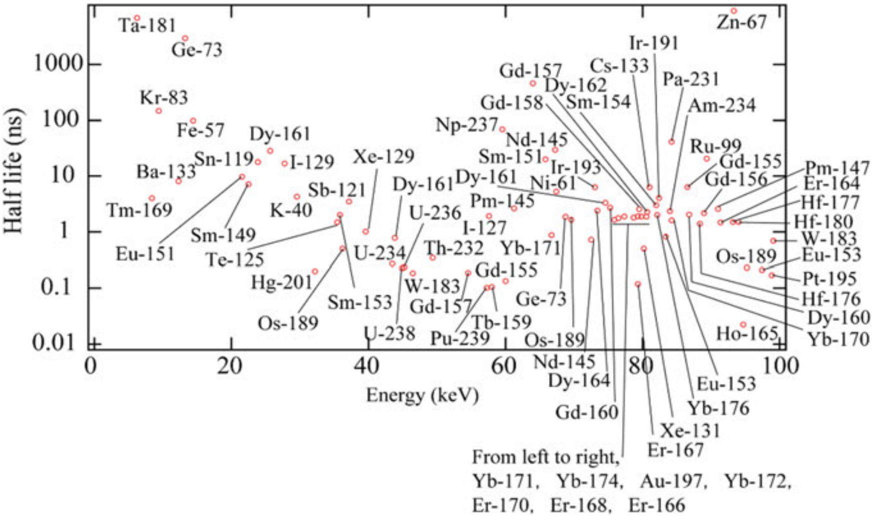

Fig. 2.2 Energy and half-life of potential Mössbauer isotopes

this method can be combined with X-ray optical techniques because of the very low angular divergence of SR and its highly polarized property. For example, the total reflection technique, which occurs in the condition of typically some milliradians, can be effectively combined and applied to Mössbauer spectroscopy of thin films.

2.2.2 *Instrumentation*

In principle, the components other than SR are as follows: monochromator(s), transmitter, scatterer, a velocity-controlling instrument (Mössbauer transducer), and a timing detector. A schematic diagram is shown in Fig. 2.3. First, SR from a beamline undulator passes through a pair monochromator Si crystal. The normal beamline monochromator usually determines the energy of SR with the bandwidth of some electron volts. This energy width is much wider than the hyperfine structure to analyze in the transmitter or scatterer in the figure. The energy modulation by the hyperfine structure is typically below some 10^{-6} eV. Thus, the energy profile of SR from the monochromator is virtually white, as shown in Fig. 2.3b. After the monochromator, the SR penetrates the transmitter in Fig. 2.3a. A sample under study or an energy reference substance at SR-based Mössbauer spectra is positioned as the transmitter. In fact, one of these two should be arranged as the transmitter, and the other should be as the scatterer. The difference between them is described later in this section.

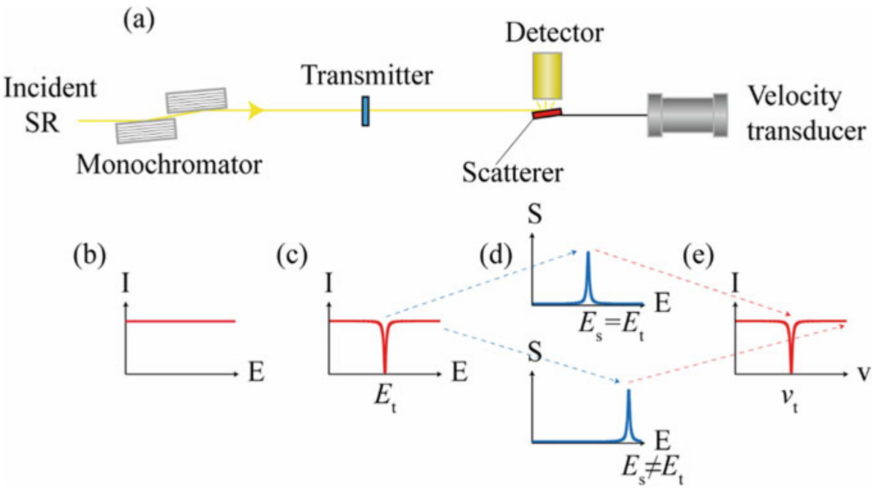

Fig. 2.3 A schematic diagram of the instrumentation and mechanism of SR-based Mössbauer spectroscopy. **a** The arrangement of instruments. **b** The energy profile of SR from the monochromator; **c** The profile of SR behind the transmitter, which has a resonant energy E; **d** The profile of the scattering from the scatterer, which has a resonant energy E_s controlled by the velocity transducer in the case of $E_s = E_t$ in the upper panel and $E_s \neq E_t$ in the lower panel; **e** The detected intensity dependence on the scatterer's velocity. At the velocity v_t, $E_s = E_t$ is satisfied

After the transmitter, SR has an energy profile reflecting the hyperfine structure of the transmitter. This situation is shown in Fig. 2.3c. Subsequently, SR is incident on the scatterer, and the scattering from the scatterer is detected by the detector, arranged just above (or below) the scatterer to cover a large solid angle from the scatterer. Here, either the transmitter or the scatterer is connected with a velocity transducer to control the nuclear resonant energy by the Doppler effect of light. Figure 2.3a shows the case in which the transducer is connected with the scatterer, and Fig. 2.3d shows the energy profile of the scattering from the scatterer, in which the resonant energy is controlled by the velocity transducer. The scatterer is usually in the shape of a plate or film and inclined to minimize the self-absorption of the scattering. At the detector, both high time response of the sub-nanosecond order and high dynamic range are required to distinguish the delayed nuclear resonant scattering from the prompt electronic scattering by setting an appropriate time window. This is because the incoherent nuclear resonant scattering was emitted with some delay corresponding to the lifetime of the excited state of the probe nuclide. Thus, we usually use an avalanche photodiode (APD) detector [24] (See 1.6.2 in this book).

A simple description of the instrumentation was presented in the previous text. In advanced cases, we have some additional components and some desirable conditions. As for monochromator, we can arrange other sets of monochromator(s) to obtain higher energy resolution. A resolution of some milli electron volts is possible by a Si crystal monochromator using higher index. Such a high-resolution monochromator drastically improves the efficiency in this method because it yields the deeper absorption spectra by suppressing non-Mössbauer nuclear resonant absorption, that is, nuclear resonant absorption with recoil. Furthermore, it also alleviates the damage to the sample. The high-resolution monochromators are available for X-rays with the energy below typically 40 keV. However, the reflectivity of such a high-resolution monochromator becomes low in higher-energy range, especially over 60 keV. Thus, we cannot always use such a monochromator. As for the transmitter and scatterer, there are some conditions. One condition is that they should not undesirably vibrate. In the measurement system, the precise control of the relative velocity between the transmitter and scatterer corresponds to the energy scan, and such undesirable vibration spoils the control. Nevertheless, the actual measurement system often includes the sources of vibration, such as vacuum pumps, refrigerators, and air compressors. Vibration from them increases the apparent energy width of the spectra and reduces their absorption depth because the spectra obtained is the convolution of the vibrational profile and the real Mössbauer spectra. When the hyperfine structure to be measured is sufficiently larger than the effect of vibration, the former effect on width might not be quite problematic, but the latter on the absorption depth is still very problematic. Therefore, the vibration should be sufficiently less than the bandwidth of nuclear levels in the velocity expression: $v_\Gamma = c\Gamma/E_{\mathrm{res}}$. Here, c denotes the speed of light, Γ denotes the natural width of the nuclear level, and E_{res} denotes the nuclear resonant energy of the nuclide. Next, we discuss the arrangement of the sample under study. It is usually more convenient to arrange the sample at the transmitter because the limitation of the transmitter in addition to the vibration control is milder than that of the scatterer. The important limitation of the transmitter is that SR penetrates

Table 2.1 List of standard references for some isotopes

Nuclides	Energy reference	Nuclide	Energy reference
^{40}K	KCl	^{125}Te	Mg_3TeO_6
^{61}Ni	$Ni_{0.86}V_{0.14}$	^{149}Sm	Sm_2O_3 or SmB_6
^{73}Ge	Li_2GeO_3 or GeO_2	^{151}Eu	EuF_3
^{119}Sn	$CaSnO_3$	^{174}Yb	YbB_{12}

it. This limitation is quite mild because the incident SR is hard X-rays. Consequently, we can arrange any environmental cells, such as a low-temperature cryostat, high-pressure cell, and gas chamber. Conversely, the limitation of the scatterer is a little complicated. The scattering from the scatterer should be efficiently detected by the detector. This limits the shape of the scatterer, as described. Nevertheless, thin film samples are sometimes good as the scatterer. As for the energy reference substance, it should be a chemical compound showing no hyperfine splitting in their resonant nuclear levels. Table 2.1 shows the chemical compounds used as suitable energy references. Some of them show small hyperfine splitting, which is not as large as the natural line width of the nuclear resonance and is not a big problem in actual use. In addition, when we perform the SR-based Mössbauer spectroscopy with isotopes whose resonant energy is high, typically above 40 keV, both the transmitter and scatterer should be cooled down to obtain a reasonable recoilless fraction. For example, the recoilless fraction of pure metal is quite different between the 14.4-keV nuclear resonance of ^{57}Fe and the 67.4-keV nuclear resonance of ^{61}Ni, although they occupy a similar position in the periodic table of elements. The recoilless fraction of nickel metal in ^{61}Ni Mössbauer spectroscopy is miserably low at room temperature, although that of iron metal in ^{57}Fe Mössbauer spectroscopy is still high at that temperature, as shown in Fig. 2.4. However, it is sometimes difficult to support both velocity control and low temperature simultaneously. One solution is to use a cryostat, where helium gas is used as a heat transfer medium. The similar effective thickness of the transmitter and scatterer is another preferable condition to obtain the spectra

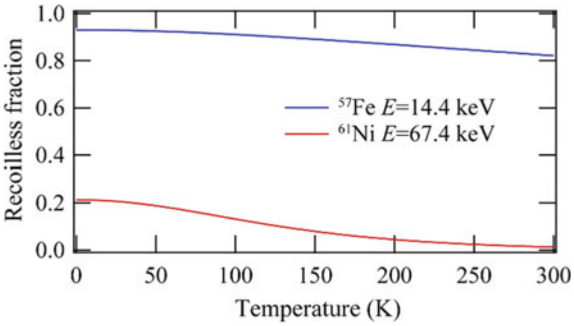

Fig. 2.4 Recoilless fraction of pure metal in ^{57}Fe and ^{61}Ni Mössbauer spectroscopy, calculated based on the Debye vibrational model. See Eq. (1.5) in Chap. 1

with reasonable absorption depth. If the scatterer is too thick, the absorption depth becomes shallow. Another condition concerns the detector. The detector usually detects scattered γ-rays, whose energy is the same as the nuclear resonant energy, and fluorescent X-rays following the internal conversion process, whose energy is lower than that of the γ-rays, as delayed nuclear resonant scattering. The detection of fluorescent X-rays becomes important in SR-based Mössbauer spectroscopy using high-resonant-energy isotopes. This is because the detection efficiency of APD becomes very low when detecting high-energy X-rays. For example, the energy of γ-rays at ^{61}Ni Mössbauer spectroscopy is 67.4 keV, while that of fluorescent Kα X-rays of Ni atom is 7.5 keV. The detection efficiency of APD, whose depletion layer is 150 μm, is 93% for the 7.5-keV X-rays and 0.9% for the 67.4-keV γ-rays. In the latest measurement system, the scatterer and detector are packed in a vacuum chamber to detect internal conversion electrons [8]. The internal conversion coefficients of many Mössbauer nuclides are higher than 1. Furthermore, the detection efficiency of the APD detector is usually 100% against electrons with energies below 100 keV. Therefore, the detection rate of the detector becomes many times higher with the electron detection in Mössbauer spectroscopy using those nuclides. For example, when a sample under an extreme condition is studied by SR-based Mössbauer spectroscopy using high-resonant-energy isotopes, the sample is often arranged in a large environmental cell and cannot be moved by a velocity transducer. Additionally, this cell blocks the internal conversion electrons. Even in that case, arranging the sample as the transmitter and the energy reference substance as the scatterer should support the following three conditions: velocity control, low temperature, and vacuum condition for the electron detection. In those cases, heat transfer by thin copper wires or springs satisfies the conditions to some extent. However, the efficiency of heat transfer by this method is usually inferior to that by the helium exchange gas technique.

2.2.3 Analysis of the Spectra

The spectra obtained are the velocity-dependent intensities and are thus very similar to the conventional Mössbauer spectra using RI. One example is shown in Fig. 2.5. A clear difference is observed between the spectra, and a simple Lorentzian evaluation was enough to see the transition in valence. In many simple cases, this kind of Lorentzian evaluation is sufficient. For this kind of rough evaluation, programs for analyzing the conventional Mössbauer spectra using RI can be applied.

However, the exact line shape of SR-based Mössbauer spectra is not Lorentzian. A deviation between the Lorentzian evaluation lines and experimental data is observed around the shoulders of absorption profiles in Fig. 2.5. Furthermore, you can see a zigzag shape at the background in the experimental data. They do not correspond to the minor component in the sample and are characteristics of SR-based Mössbauer spectra, caused by the measurement method described above. They depend on some factors, such as the effective thickness of the transmitter and the scatterer, chemical composition, and time window at the APD detector. Now, we consider the detailed

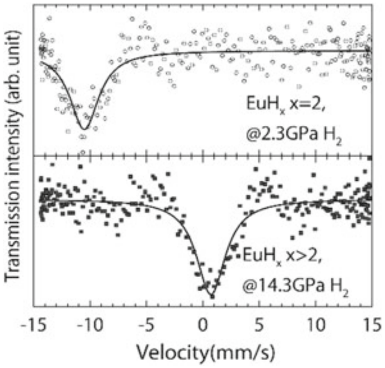

Fig. 2.5 ^{151}Eu SR-based Mössbauer spectra of Eu metal under high *hydrogen* pressure. The energy reference substance was EuF_3 as the scatterer. Rectangles represent experimental data, and lines represent fitting curves by Lorentzian shape. The upper panel shows the Eu^{2+} valence under 2.3 GPa hydrogen, and the lower panel shows Eu^{3+} valence under 14.3 GPa hydrogen (reproduced from Matusoka et al. (2011) [25])

expression on these characteristics [26]. For simplicity, we assume the following conditions: (1) the transmitter is a sample under study and includes only one chemical compound with one site and (2) the scatterer is an energy reference substance and connected to the velocity transducer, as shown in Fig. 2.3. Our aim here is to express the detected intensity as a function of the velocity of the scatterer. First, the propagating coherent field amplitude of the transmitter E_t as a function of the dimensionless frequency of w, that is, in the unit of natural linewidth, is considered. It corresponds to the absorption by electrons and nuclei in the transmitter and is expressed as follows:

$$E_t(w) = E_{0t}\exp\left(-\frac{\mu_{et}z_t}{2}\right)\exp\left(-i\sum_m \alpha_{tm}\frac{\mu_{nt}z_t}{2(2(w-w_{tm})+i)}\right). \qquad (2.1)$$

Here, the amplitude of the radiation field at the entrance of the transmitter is denoted as E_{0t}. The electronic absorption coefficient of the transmitter is denoted as μ_{et}. The thickness of the transmitter is denoted as z_t. The linear absorption coefficient of radiation by the nuclei at resonance in the transmitter is denoted as μ_{nt}. The index for a nuclear transition is denoted as m. The probability and the nuclear resonant energy of the mth transition at the transmitter are denoted as α_{tm} and w_{tm}, respectively. The hyperfine structure of the transmitter, which is described by isomer shift, quadrupole splitting, and magnetic hyperfine field, is expressed as w_{tm}. The purpose of Mössbauer spectroscopy is to evaluate them. Here, $\mu_{nt}z_t$ corresponds to Mössbauer effective thickness T_t. Next, the propagating coherent field amplitude of the scatterer E_s as a function w is considered. It also corresponds to the absorption by electrons and nuclei in the scatterer and is expressed as follows:

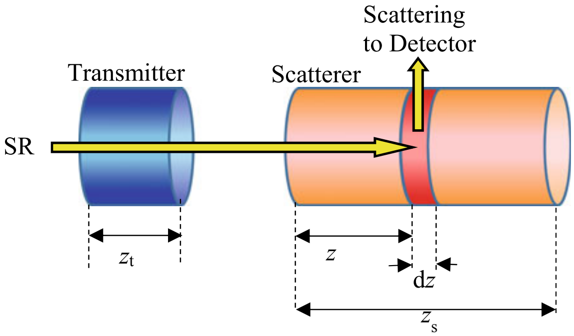

Fig. 2.6 A schematic diagram of parameters used for the detailed expression of SR-based Mössbauer spectra

$$E_s(w, w_s, z) = E_{0s}\exp\left(-\frac{\mu_{es}z}{2}\right)\exp\left(-i\frac{\mu_{ns}z}{2(2(w - w_s) + i)}\right). \tag{2.2}$$

Here, w_s denotes the nuclear resonant energy of the scatterer, and z denotes the depth to which SR penetrates as indicated in Fig. 2.6. The other variables denote similarly to those of the transmitter, although the suffix "t" should be changed to "s," which denotes the scatterer. Equation (2.2) is expressed as a function of w, w_s, and z because w_s is controlled by the velocity transducer and w and z are used for the calculation in the following equations. This field was absorbed by the scatterer at the depth z, as described in the following step, and thus, z is less than the thickness of the scatterer z_s. Because the energy reference substance is assumed at the scatterer, hyperfine splitting is absent, and the summation of the nuclear transition index m is not described. Subsequently, we consider the scattering process at the scatterer. Here, it is enough to consider the w_s-dependent processes, which are as follows: (1) the emission following the recoilless nuclear resonant absorption of radiation and (2) the scattering of the radiation due to the photoelectric absorption. Here, we call the former process as channel A and the latter as channel C according to [26]. In channel A, SR penetrates the transmitter and scatterer until the depth z and is then resonantly absorbed. In this channel, the scattering field $E_A(w, w_s, z)$ satisfies

$$E_A(w, w_s, z) \propto \frac{1}{w - w_s + i/2}E_t(w)E_s(w, w_s, z).$$

Now, we can obtain the detected intensity $I_A(w_s)$ as follows:

$$\begin{aligned} I_A(w_s) &= C_A\int_{\tau_1}^{\tau_2}\mathrm{d}\tau\int_0^{z_s}\mathrm{d}z\left|\int\frac{\mathrm{d}w}{2\pi}\exp(-iw\tau)E_A(w, w_s, z)\right|^2 \\ &= C_A\int_{\tau_1}^{\tau_2}\mathrm{d}\tau\int_0^{z_s}\mathrm{d}z\left|\int\frac{\mathrm{d}w}{2\pi}\frac{\exp(-iw\tau)}{w - w_s + i/2}E_t(w)E_s(w, w_s, z)\right|^2, \end{aligned} \tag{2.3}$$

where C_A denotes a proportionality factor. This expression includes (1) the Fourier transformation of $E_A(w, w_s, z)$ to obtain the time dependence of E_A and the square of its magnitude to obtain the intensity from the field and (2) the integrations on the depth z and τ; the τ integration corresponds to the time window at APD. In channel C, NFS by the transmitter or scatterer is scattered by electrons at depth z. Thus, the incident field at the depth satisfies

$$E_{\mathrm{C}}(w, w_{\mathrm{s}}, z) \propto 1 - E_{\mathrm{t}}(w) E_{\mathrm{s}}(w, w_{\mathrm{s}}, z).$$

Considering cross section of electrons independent of w_{s}, the detected intensity $I_{\mathrm{C}}(w_{\mathrm{s}})$ is obtained as

$$\begin{aligned} I_{\mathrm{C}}(w_{\mathrm{s}}) &= C_{\mathrm{C}} \int_{\tau_1}^{\tau_2} \mathrm{d}\tau \int_{0}^{z_{\mathrm{s}}} \mathrm{d}z \left| \int \frac{\mathrm{d}w}{2\pi} \exp(-iw\tau) E_{\mathrm{C}}(w, w_{\mathrm{s}}, z) \right|^2 \\ &= C_{\mathrm{C}} \int_{\tau_1}^{\tau_2} \mathrm{d}\tau \int_{0}^{z_{\mathrm{s}}} \mathrm{d}z \left| \int \frac{\mathrm{d}w}{2\pi} \exp(-iw\tau)(1 - E_{\mathrm{t}}(w) E_{\mathrm{s}}(w, w_{\mathrm{s}}, z)) \right|^2, \end{aligned} \tag{2.4}$$

where C_{C} denotes another proportionality factor. Now, we have the expression of the detected intensity $I(w_{\mathrm{s}})$ as

$$I(w_{\mathrm{s}}) = I_{\mathrm{A}}(w_{\mathrm{s}}) + I_{\mathrm{C}}(w_{\mathrm{s}}) + I_{\mathrm{B}}, \tag{2.5}$$

where I_{B} denotes for other processes independent of w_{s}, such as the process with nuclear resonant scattering with recoil at the scatterer (called channel B).

The narrowing of the energy width and the wavy pattern in the background are now discussed based on Eqs. (2.1)–(2.5). The narrowing effect depends on the time window, as shown in Fig. 2.7. Here, a narrower energy width was obtained compared to the ideal linewidth in conventional Mössbauer spectroscopy, which is twice the natural linewidth. For example, although the ideal linewidth is 2.0 mm/s in conventional ^{174}Yb Mössbauer spectroscopy, a full-width at half maximum (FWHM) of 1.3 mm/s was achieved [8]. This property is advantageous when the nuclear hyperfine structure is small and precise analysis is required. In contrast, the wavy pattern in the background is usually a drawback because it may conceal small components in the spectra, at least in the initial guess for analysis. Proper analysis using the equations is required. Note that if the time window is [0, ∞], both the narrowing effects and the wavy background vanish. In addition to the [0, ∞] time window, in the case of thin transmitter and scatterer, the spectra show Lorentzian shape with the "ideal linewidth," similar to the conventional Mössbauer spectroscopy using RI. Therefore, the Lorentzian approximation described at the beginning of this section corresponds to the case. These situations are similar to the delayed coincidence Mössbauer spectroscopy using RI [27, 28]. Furthermore, the equations also show better conditions for the measurement system, described previously. For example, the high-resolution monochromator enhances the absorption depth of the spectra because it suppresses the channel B process. Furthermore, the effective thickness of the transmitter and that of scatterer (i.e., the sample and energy reference) should be similar.

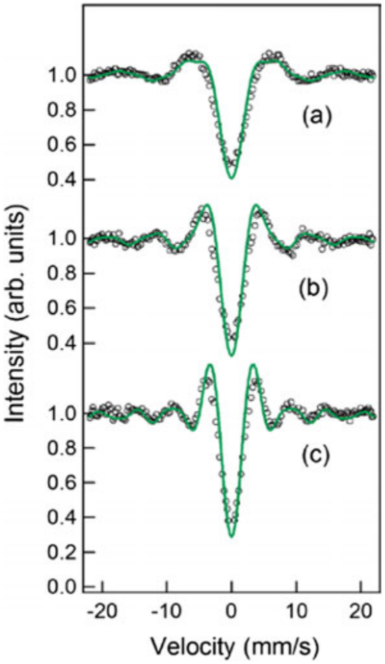

Fig. 2.7 SR-based Mössbauer absorption spectra of ^{151}Eu with the following time windows: **a** 5.7–17.0 ns, **b** 8.1–17.0 ns, and **c** 10.5–17.0 ns. The transmitter and scatterer were EuF_3. Lines are the spectra calculated by Eqs. (2.1)–(2.5) (reproduced from Seto et al. (2010)) [22]. Note that the lifetime $\tau_{151\mathrm{Eu}} = 14$ ns

To calculate the above equations, parameters on the isotopes and elements are necessary. Fortunately, we have many databases of them. One good source is the Mössbauer Effect Data Center [9]. For nuclear data, the Table of Isotopes [29] and the National Nuclear Data Center website [30] are also excellent sources. Electronic absorption coefficients are shown in the web database by Sasaki [31] and the National Institute of Standards and Technology (NIST) website [32] based on [33, 34].

We should also consider the type of scattering that the APD detects because the absorption rate of γ-rays, internal conversion electrons, and fluorescent X-rays following the internal conversion processes are different. Particularly, the stopping power of electrons is much higher than those of the other two. Even 100-keV electrons cannot penetrate an aluminum plate of 70 μm. The penetration length can be calculated according to [35] and seen in the web database by NIST [36] based on [37].

Another subject in the analysis of SR-based Mössbauer spectra of various isotopes is the interpretation of the hyperfine structure parameters: the sets of isomer shift, quadrupole splitting, and magnetic hyperfine field. Although many chemical compounds have been studied using ^{57}Fe and ^{119}Sn Mössbauer spectroscopy, few compounds have been studied using other isotopes. Even so, the preceding studies, including experiments by NFS and conventional Mössbauer spectroscopy will help the analysis. A substantial description on various isotopes by Greenwood and Gibb [2], Shenoy and Wagner [38], and Gütlich et al. [39] can be very useful.

2.2.4 Comparison with Other Methods Using SR

Here, the properties of the SR-based Mössbauer spectroscopy are compared with those of the SMS and NFS, the two major methods to observe the hyperfine structure of samples using SR. These methods are in a complementary relation. The differences in these methods described here will help in selecting the best method for a study.

As for the SMS, energy-domain spectra are obtained similarly to SR-based Mössbauer spectroscopy. One large difference between the two is the nuclide availability. In the SMS, a unique component produces Mössbauer radiation, that is, SR whose energy width is as narrow as the natural linewidth of a Mössbauer isotope. This component is a nuclear monochromator at which the nuclear diffraction is allowed, although the usual diffraction by electrons is prohibited [40]. Nuclear monochromator is successfully developed only for ^{57}Fe, and thus, the SMS is limited to ^{57}Fe Mössbauer spectroscopy, which is different from SR-based Mössbauer spectroscopy, in which many isotopes can be used. Furthermore, the nuclear monochromator produces Mössbauer radiation without a time window, and thus, the SMS method has no limit on the time structure on SR in principle. SR-based Mössbauer spectroscopy requires at least some kind of pulsed time structure of SR with the time period for the time window by which the delayed nuclear resonant scattering is selected. Although this difference is only a technical point, it is important to the actual experiment because various bunch modes exist in SR facilities. Neither width-narrowing effect nor the wavy background is seen in the SMS, and thus, the analysis of the SMS spectra is usually more intuitive.

As for the NFS, the hyperfine structure of various isotopes can be observed by both NFS and SR-based Mössbauer spectroscopy. A large difference is noticeable in the appearance of the spectra. The time spectra showing beat patterns due to the interference of nuclear hyperfine splitting at the sample are obtained in NFS. Therefore, NFS is suitable in tracing a reaction depending on the time in the scale of nanoseconds, such as pump-probe spectroscopy. For stable samples, this difference in appearance affects the analyzing model at an initial guess: the energy spectra of SR-based Mössbauer spectroscopy are intuitive. When there are two or more components in the sample, this intuition becomes important. In the experimental viewpoint, NFS requires an appropriate time structure of SR to obtain the time spectra. This limitation is stricter in NFS than in SR-based Mössbauer spectroscopy. The required period between SR pulses in NFS depends on the magnitude of hyperfine splitting to be evaluated. However, the magnitude is not usually obvious. In actual experiments, the period with more than the lifetime of the nuclear excited state is usually enough (the longer the period, the better). This limitation sometimes restricts isotope availability. When we have the suitable timing bunch mode of SR facility, the measuring time tends to be shorter in NFS because the interference pattern of all nuclear levels by hyperfine splitting is measured in the time region without any energy-scanning mechanism. In contrast, the energy dependence of the scattering intensity is measured with the mechanical motion of the energy reference substance in SR-based Mössbauer spectroscopy. The efficiency of the measurement system in NFS is somewhat small in experiments with high-resonant-energy isotopes owing to the detection efficiency of the APD. Only high-energy γ-rays from the sample should be detected in NFS, while low-energy fluorescent X-rays and electrons after the internal conversion processes from the scatterer could be also detected in SR-based Mössbauer spectroscopy. Additionally, it is sometimes difficult to obtain the interference pattern in the time spectra of NFS when the lifetime of the nuclear excited level of the probe isotope is short. In those cases, SR-based Mössbauer spectroscopy is preferable. Thus, SR-based Mössbauer spectroscopy suits Mössbauer spectroscopy using nuclear levels, whose energy is high and whose lifetime is short.

2.3 Nuclear Resonant Inelastic Scattering

While Mössbauer spectroscopy uses the recoilless nuclear resonant excitation effect, the energy tunability of SR enables the measurement of the recoil part. Therefore, nuclear resonant excitation accompanied by phonon excitation can be measured using SR. Hence, the first experiment was performed in 1994 [5], and phonon measurement was conducted [41, 42]. The NRIS method has distinct features favorable for studies concerning the microscopic dynamics (e.g., phonons and molecular vibration) of materials because it provides the element (isotope)-specific dynamics due to the resonant excitation of the specific isotope. In solids, partial phonon densities of states are measured. Furthermore, measurements under extreme conditions, such as high pressures, small samples, and thin films, are possible because of the high brilliance of SR. (For the definition of brilliance, see Chap. 1.) Note that the element (isotope)-specific nature enables the measurement of very dilute resonant atoms in complicated materials. Recently, this method has been actively used to study the local structure of active sites in enzymes along with first-principles density functional theory (DFT).

2.3.1 Instrumentation and Analysis of the Basic Method of NRIS

The measurement is performed through inelastic processes with photons. The energy of each photon is equal to the sum of the energy of the nuclear resonant excited state (based on the ground state) and a phonon (or phonons). Since the typical energy of phonon is 1–100 meV, spectroscopic resolution required for the measurement is approximately several mill electron volts or less. Usually, SR produced by an undulator installed in a recent hard X-ray storage ring is approximately several electron volts, and it is possible to generate X-rays with a bandwidth of approximately several milli electron volts (in special cases, approximately 0.1 meV can be achieved [43]) using Si monochromators. Sapphire (α-Al_2O_3), a material for the monochromator, in addition to Si, has been used particularly for high-energy nuclides [44, 45]. The incident energy can be scanned at approximately the nuclear resonant excitation energy by changing the Bragg angle of the monochromator. Note that the respective nuclear resonant energies of the available isotopes are much more than the usual scan range (100 meV). Therefore, pure element (isotope)-specific measurement is assured.

To observe the phonon energy spectrum, we irradiate a sample containing the resonance isotope as a function of the energy of the generated X-rays with a bandwidth of approximately several milli electron volts. From the irradiated sample, a strong scattering is emitted due to photoelectron effects and so on. Therefore, to discern the relatively weak nuclear scattering from the strong scattering, we observe only delayed photons (e.g., fluorescence X-rays and γ-rays) and electrons (e.g., conversion electrons) emitted at the de-excitation in the time domain because scattering due to electronic processes is promptly emitted at the irradiation. The schematics of the measurement of nuclear resonant excitation accompanied by phonon creation or annihilation are shown in Fig. 2.8. As shown in the figure, if the energy of the incident photon is equal to the sum of the energy of the nuclear resonant excited state and a phonon, one phonon is created. Alternatively, one-phonon annihilation occurs if the sum of the energy of the incident photon and that of a phonon is equal to the sum of the energy of the nuclear resonant excited state. The detection system with a closed-cycle refrigerator cryostat for NRIS measurement using an eight-element APD detector is shown in Fig. 2.9.

We can obtain the phonon density of states (PDOS) weighted by the projection of the polarization vectors on the direction of the incident X-ray radiation from the NRIS measurement. Based on [46], the following expression is relevant:

$$g(E, \boldsymbol{\kappa}) = \frac{V}{(2\pi)^3} \sum_j \int d\mathbf{q} \left| \boldsymbol{\kappa} \cdot \mathbf{e}_j(\mathbf{q}) \right|^2 \delta\left(E - \hbar\omega_j(\mathbf{q})\right), \tag{2.6}$$

where V is the volume of the unit cell, $\mathbf{q}$ is the phonon wave vector, ω_j ($\mathbf{q}$) is the phonon dispersion relation for the branch j, $\boldsymbol{\kappa}$ is the normalized wave vector of the incident X-ray ($\boldsymbol{\kappa} = \mathbf{k}/|\mathbf{k}|$, $\mathbf{k}$: wave vector of incident X-ray), and $\mathbf{e}_j$ ($\mathbf{q}$) is the polarization vector of the vibrations of the resonant atom. For single crystals with a cubic Bravais lattice and polycrystalline materials composed of resonant atoms only, $g(E, \boldsymbol{\kappa})$ is the exact PDOS. In the general case of a polycrystalline material, that is, a material composed of not only resonant atoms but also other nonresonant atoms, averaging over all directions of the incident radiation results in $g(E)$, representing a PDOS weighted by the square amplitude of the resonant atoms. Therefore, we can obtain a partial PDOS for a specific element (isotope). The nuclear resonant inelastic absorption cross section can be expressed using the following weighted PDOS:

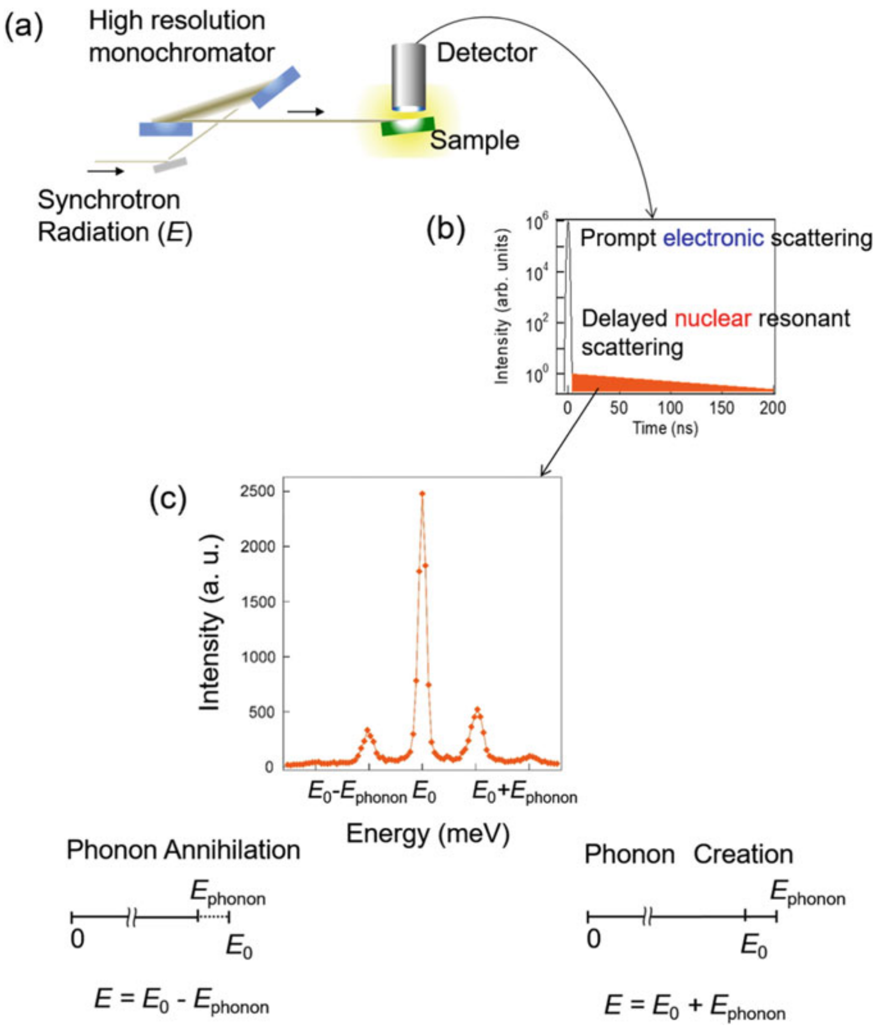

Fig. 2.8 **a** Schematic diagram for the measurement of nuclear resonant inelastic scattering. **b** Nuclear resonant scattering is discerned from prompt electronic scattering in the time domain as delayed scattering because of the finite lifetimes. **c** As a function of the incident photon energy E, the phonon energy spectrum can be obtained by counting the intensity of delayed scattering. In the phonon energy spectrum, the left-side scattering is due to the excitation accompanied by phonon annihilation [$E = E_0$ (nuclear resonant excitation energy) - E_{phonon} (phonon energy)], while the right-side scattering is due to excitation accompanied by phonon creation [$E = E_0 + E_{\mathrm{phonon}}$]

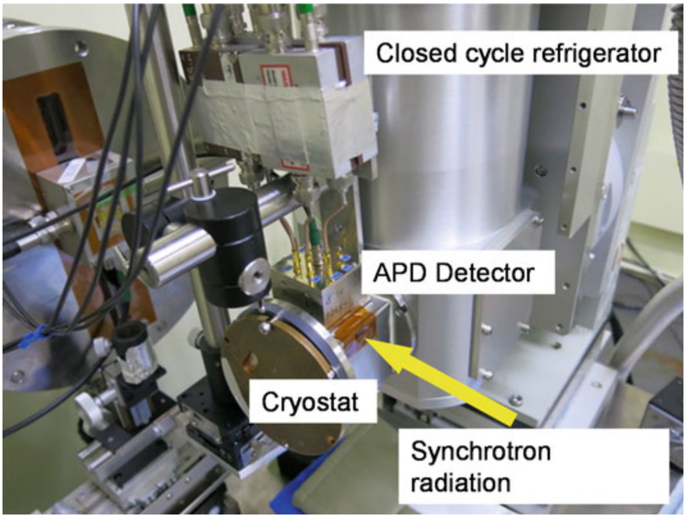

Fig. 2.9 Photograph of the detection system for nuclear resonant inelastic scattering measurement using an eight-element avalanche photodiode (APD) detector. The sample in a cryostat chamber can be cooled with the closed cycle refrigerator

$$\sigma_a(E) = f_{LM} \int \frac{d\tau}{2\pi} \exp(-\mathrm{i}E\tau)\big[\exp(M(\mathbf{k},\tau)) - 1\big], \tag{2.7}$$

where

$$M(\mathbf{k},\tau) = \int dE \, \exp(\mathrm{i}E\tau) S(E,\mathbf{k}), \tag{2.8}$$

$$S(E,\mathbf{k}) = E_R \, g(E,\boldsymbol{\kappa}) \frac{\overline{n}+1}{E}, \tag{2.9}$$

$$f_{LM} = \exp(-M(\mathbf{k},0)), \tag{2.10}$$

$$E_R = \frac{(\hbar\mathbf{k})^2}{2M}, \tag{2.11}$$

$$\bar{n} = (\exp(E/k_{\mathrm{B}}T) - 1)^{-1}. \tag{2.12}$$

In the above expressions, M is the mass of the resonant nucleus and k_{B} is the Boltzmann constant. Using Fourier transformation of the cross section corresponding to the measured spectrum, $g(E, \boldsymbol{\kappa})$ can be obtained through $M(\mathbf{k},\tau)$ and $S(E,\mathbf{k})$, as shown in Eqs. (2.7) and (2.8). However, before performing these procedures, the subtraction of the elastic peak and the deconvolution of the monochromator widths are required. Since the perfect deconvolution is impossible for the real measured spectrum containing statistical and other errors, the obtained $g(E, \boldsymbol{\kappa})$ sometimes contains the apparent broadening due to the monochromator width. Moreover, special care should be given to this behavior at low-energy region within the monochromator width due to the subtraction. In Fig. 2.10, the obtained PDOS from measured NRIS spectrum is shown using these processes. These procedures are precisely described in [47, 48]. The area ratio of the elastic peak to the total part in the NRIS spectrum as shown in the upper spectrum of Fig. 2.10 may be considered as the recoilless fraction, which is known as the Lamb–Mössbauer factor in Mössbauer spectroscopy. However, it may be incorrect because coherent forward scattering occurs at the exact nuclear resonant energy, while such coherent scattering does not, besides the resonant energy, as discussed in Chap. 1. Although the recoilless fractions are sometimes required to compare the Mössbauer results, PDOS has much better information and gives the recoilless fraction value [47].

In eq. (2.12), $\bar{n}$ indicates Bose factor ruling the temperature dependence of the spectrum. Since phonon is boson, phonon creation is proportional to $\bar{n} + 1$, which is shown in eq. (2.12), while phonon annihilation is proportional to $\bar{n}$. As $\bar{n}$ approaches

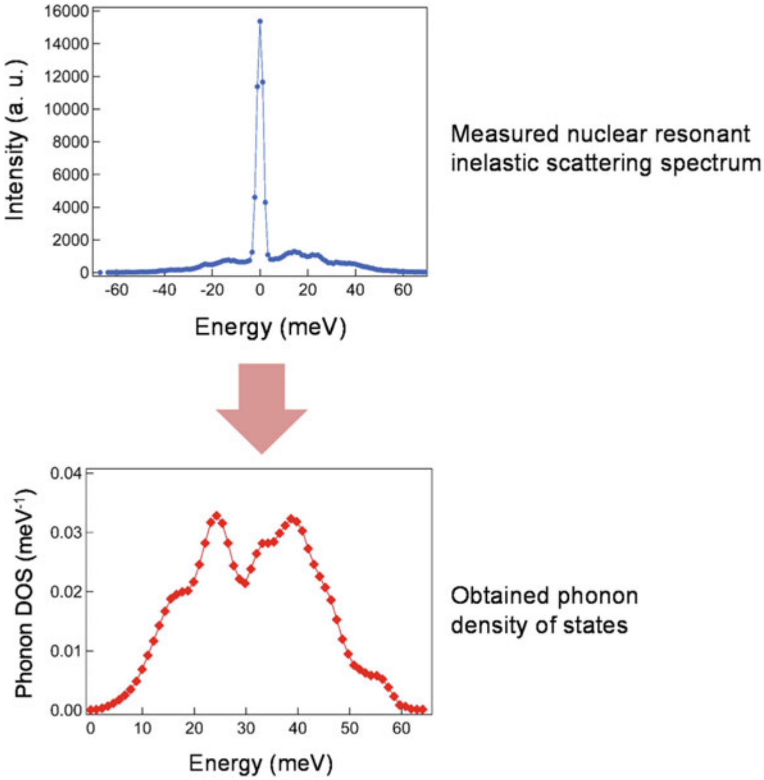

Fig. 2.10 Phonon density of states shown in the spectrum below is obtained from the measured nuclear resonant inelastic scattering spectrum shown above [49]

to zero by lowering the temperature to zero, phonon annihilation is difficult to observe at low temperature as expected. In contrast, phonon creation is possible even at zero temperature as seen in eq. (2.9). Therefore, the asymmetry of the phonon energy spectrum is observed at low temperatures. The NRIS spectra of ^{57}Fe in superconductor LaFeAsO$_{0.89}$F$_{0.11}$ at 298 K and 15 K are shown in Fig. 2.11 [50]. Note that this method does not provide phonon dispersion relations, which can be obtained from other relevant methods, such as inelastic neutron and X-ray scattering methods, but does provide measurements of polycrystalline, disordered, and amorphous materials. Furthermore, an ideal partial PDOS averaged over phonon momenta can be obtained by observing the emissions due to the nonradiative channel of nuclear de-excitation.

This element-specific phonon information is important because the dynamics of certain atoms in a compound sometimes influence the characteristics of the compound. Therefore, the NRIS of SR that provides element (isotope)-specific phonon energy spectra is advantageous. Moreover, in this method, it is possible to study the dynamics of highly diluted impurities or doped atoms in metals and semiconductors. In Fig. 2.12a, the local PDOS of Fe (0.017 at.%) in Al metal measured by NRIS of SR is shown [51], and the PDOS of Al metal, obtained from a neutron inelastic scattering experiment [52], is also shown in Fig. 2.12c for comparison. A clear difference between the PDOS of ^{57}Fe in Al and that of the Al metal host can

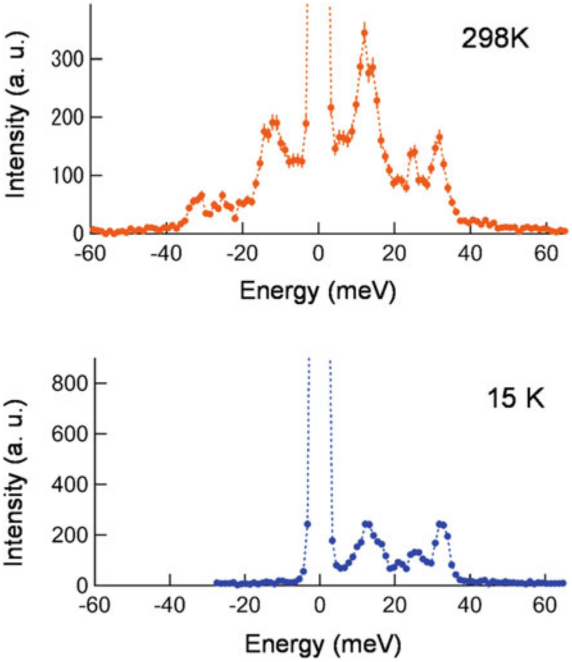

Fig. 2.11 Asymmetry of the phonon energy spectrum is observed at low temperature as shown in the nuclear resonant inelastic scattering spectra of ^{57}Fe in superconductor LaFeAsO$_{0.89}$F$_{0.11}$ at 298 K and 15 K [50]

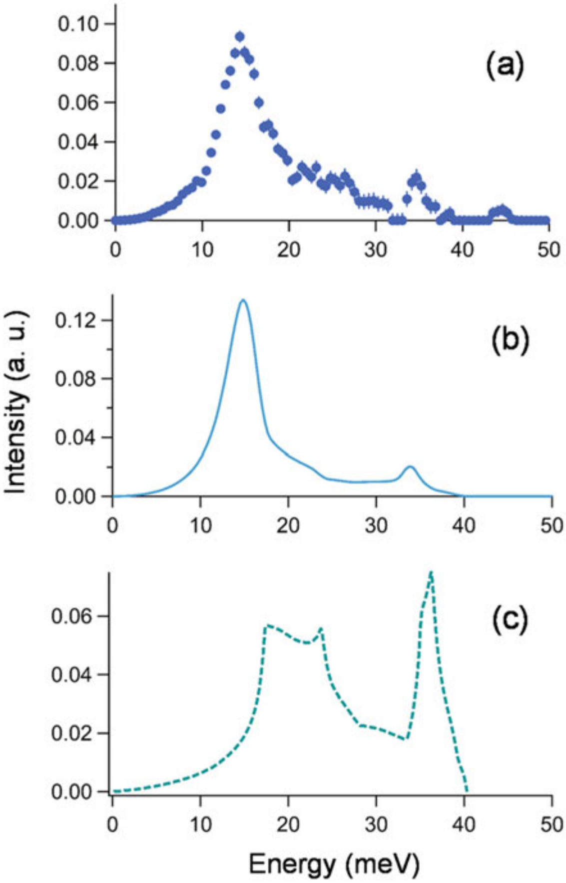

Fig. 2.12 **a** Phonon density of states (PDOS) of ^{57}Fe in Al-0.017 at.% Fe [51]. **b** Response function of the impurity Fe atom to the PDOS of Al metal calculated on the basis of Mannheim's impurity theory [53]. **c** PDOS of Al [52]

be seen by comparing Fig. 2.12a and c. The reliability of the observed spectrum was confirmed using a Green function method that can reproduce the local PDOS from that of the host metal and the coupling between the impurity and host atoms [53]. The phonon spectrum calculated using this method is shown in Fig. 2.12b. It is shown that the calculation well reproduces the measured PDOS of Fe (Fig. 2.12a). The characteristic vibrational modes of Fe in Al were found to be modes that vibrate resonantly with the host Al phonons. Although the measurement of the PDOS of diluted atoms is quite difficult, this method gives clear and reliable results.

2.3.2 Examples of Frontier Science, Especially Biological Application

Element (isotope) selectivity is very advantageous when the function and local structure of a specific atom in a complex compound are of interest. Resonant Raman spectroscopy provides valuable information on the vibrational properties of samples, such as metalloprotein samples. Furthermore, it has been used effectively. However, the selection rule sometimes hampers the observation of vibrational modes. In contrast, NRIS method gives all modes that involve motion of the resonant nuclei. Therefore, it provides the opportunity to study the ligation and oxidation state of a specific site. Many studies have been conducted to determine the vibrational amplitudes and frequencies for specific atoms in a complex biological macromolecule without selection rules using the isotope selectivity (for example [54–76]). In particular, this method has been used to study specific sites in large molecules, such as metalloprotein samples, involving thousands of other atoms. The investigation of the structure around the specific site of interest is conducted by comparing the obtained phonon energy spectrum with the vibrational spectrum obtained from DFT calculations under the assumption of the presumable structural model. This method is effective for samples that cannot be crystallized, such as the intermediates in the catalytic cycles of enzymes. Furthermore, the structural characterization of the reactive $\mathrm{Fe(IV)} = \mathrm{O}$ intermediate in the catalytic cycles of a mononuclear non-heme iron (NHFe) enzyme (the halogenase SyrB2 from the bacterium *Pseudomonas syringae* pv. *syringae*) was studied (Fig. 2.13) [72]. The intermediate reacts through an initial hydrogen-atom abstraction step and performs subsequent halogenation of the native substrate or hydroxylation of nonnative substrates, Therefore, the revelation of its local structure and mechanism is quite essential and important. In this study, it was indicated that the orientation of the $\mathrm{Fe(IV)} = \mathrm{O}$ intermediate depends on the substrate, presenting specific frontier molecular orbitals responsible for hydrogen-atom abstraction that can selectively lead to halogenation or hydroxylation. Moreover, NRVS was used in studying the catalytic mechanism of hydrogenases, which catalyze the reversible conversion of molecular hydrogen to protons and electrons. Understanding the mechanism is quite significant because it leads to the development of clean energy sources in producing hydrogen. NRVS was applied to [FeFe] hydrogenase variant lacking the amine proton shuttle, which is stabilizing a putative hydride state [75]. [FeFe] hydrogenases are metalloenzymes that reversibly reduce protons to molecular hydrogen with extremely high efficiency. NRVS spectra clearly showed the bending modes of the terminal Fe–H species that is consistent with the widely accepted models of the catalytic cycle.

The high brilliance of SR allows the PDOS even for small samples to be measured. For example, measurements under extreme conditions in which the accessible sample space is severely limited are possible. The PDOS under high pressures using a diamond anvil cell (DAC), where the sample size is typically less than 1 mm^2, is measured to study the core of the earth [77–79]. Additionally, many important studies using the features of NRIS spectroscopy have been conducted, for example,

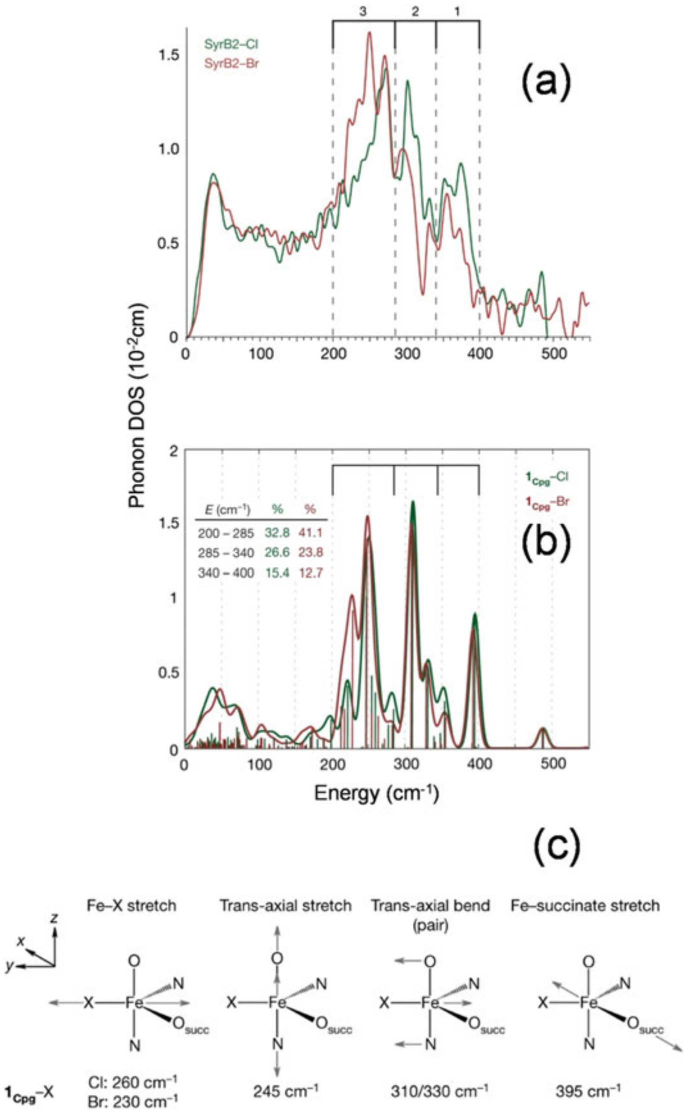

E (cm^{-1})	%	%
200 – 285	32.8	41.1
285 – 340	26.6	23.8
340 – 400	15.4	12.7

Fig. 2.13 **a** Phonon densities of states of SyrB2–Cl and SyrB2–Br. **b** DFT-predicted the phonon densities of states. **c** DFT-predicted four normal modes of the five-coordinate Fe(IV) = O structure [72]

on nanoparticles [80–85], thin films [86–92], quasicrystals [93], clathrates [94, 95], superconductors [50, 96–98], filled skutterudites [99, 100], and glass [101, 102]. The nuclear resonant scattering method can be applied to not only solids but also liquids. The element-specific diffusion constant of Fe ions in HCl solution [103] and the dynamics of Fe ions in Nafion membranes [104, 105] were measured using the aforementioned method, which are used as ion-exchange membranes.

This method gives element (isotope)-specific phonons but there are compounds containing two or more different atomic states of a particular element; for example, magnetite, which is a mixed-valence Fe compound, is well-known [106]. Although this method cannot distinguish the "site-specific" vibrational properties, information on the difference of the sites is sometimes required because the properties of the individual atomic motion in nonequivalent positions in a compound are not necessarily equivalent; in fact, mixed valence systems, such as iron oxides with a phase transition accompanied by charge splits [107], and spin crossover materials [108], are well known. Furthermore, even in an ideal material containing only one atomic site, there may be atoms with different environments due to imperfections or impurities. Materials with different sites occupied by the same element are not unusual. A method capable of distinguishing the vibrational properties of a specific site is valuable and crucial.

2.3.3 Advanced NRIS Method

Thus far, the measurement of electronic and phonon states has been studied independently, except for the information on the recoilless fraction of the Mössbauer effect. The recoilless fraction sometimes gives important insights for the lattice dynamics study. However, PDOS, which allows us to calculate the recoilless fraction as discussed above, has quite rich information. The combination of the measurement methods of phonon energy spectra and incoherent time spectra through the hyperfine interactions permits the observation of the site-specific PDOS [6]. Since the observed NRIS consists of scattering from individual excited nuclei, the PDOS obtained from the scattering spectrum is the sum of the partial PDOS of individual atoms. Therefore, a partial PDOS of each atom is obtained from the measured NRIS spectrum by discerning the contribution of each atom. The hyperfine interactions between the nuclei and the surrounding electronic states, which split the nuclear energy level, allow this procedure. In that case, quantum beats whose oscillating cycles reflect the splitting energies are observed in the time-domain measurement of incoherently emitted γ-rays during the decay of an excited nucleus. The incoherently emitted γ-rays obey an exponential law with a finite lifetime. In the case of multiple electronic states of a certain element in a compound, the hyperfine interactions for those states are different, and the beat patterns in the time spectrum are expected to be different. The measurement of the quantum beat patterns enables the identification of the respective electronic states and gives the component ratios of the sites. If the nuclear resonant excitation accompanied by phonon excitation occurs at a certain incident radiation energy, the analysis of the quantum beat pattern in the time spectrum reveals the respective phonon contributions from those sites with different electronic states. Performing this procedure at different energies allows us to observe the partial PDOS as distinguished by electronic states.

Using this method, the site-specific PDOS in magnetite (Fe_3O_4) was measured. In magnetite, which is a well-known mixed-valence compound, the iron atoms are located in two nonequivalent positions in the unit cell. One-third of the Fe ions (Fe^{3+}) occupy the A sites and are tetrahedrally surrounded by four oxygen ions. The remaining two-thirds of the Fe ions (Fe^{3+} and Fe^{2+}) occupy the B sites and are octahedrally surrounded by six oxygen ions. Magnetite is ferrimagnetic, and the magnetic moments of the A sites are aligned antiparallel to the magnetic moments of the B sites below T_N=858 K. Nuclear magnetic resonance spectroscopy and Mössbauer spectroscopy cannot distinguish the Fe^{3+} or Fe^{2+} ions on the B sites, indicating the delocalized nature of the charge carriers with a formal average valence of $Fe^{2.5+}$ at room temperature [106]. The sample measured in this experiment was prepared such that oxidization is prevented and was doped with 7 mol% Ni to replace Fe because some B sites are probably oxidized to Fe^{3+} in air [109]. The enrichment of ^{57}Fe in the used sample was 95.5%. The energy spectrum of NRIS of ^{57}Fe in Fe_3O_4 is shown in Fig. 2.14a. Examples of the incoherent time spectra (measured at 16 meV and 35 meV) are shown in Fig. 2.14b [6]. From these time spectra, the ratio of A site and B site at each phonon energy was obtained by least-squares fitting each time spectrum with two exponential functions accompanied by sinusoidal quantum beats corresponding to A and B sites. These ratios and the PDOS of all Fe atoms give the partial PDOSs of A site and B site. The obtained spectra of the partial PDOS for all Fe sites and the site-specific PDOSs of the A and B sites are shown in Fig. 2.15a. The difference between the partial PDOS s of the A and B sites is clearly observed. In Fig. 2.15b, the PDOSs of Fe in the ideal Fe_3O_4 obtained from ab initio band calculations are shown. The PDOS of all Fe is shown as a black line, and the calculated PDOSs of states of the A and B sites are shown as dashed green and dashed-and-dotted dark yellow lines, respectively. The overall character of the calculated PDOS of all Fe sites in Fe_3O_4 agrees well with the PDOS of all Fe sites measured by NRIS spectroscopy. Neutron inelastic scattering, X-ray inelastic scattering, Raman scattering, and infrared absorption methods are well-known and very useful for the study of atomic dynamics. It is, however, generally impossible to discern the atomic motions of the same element in different environments. Therefore, this method is considered to be unique.

2.3.4 Summary

NRIS spectroscopy is a method used for investigating the vibrational states in substances. Since NRIS spectroscopy uses the nuclear resonant excitation accompanied by phonon creation and annihilation, unique and very effective measurement is possible as shown above. The development of spectroscopic methods is ongoing, and remarkable progress has been achieved in relation to the optics, detectors, and methodologies used. Because this spectroscopy covers a broad range of scientific areas, such as physical, chemical, biological, and earth sciences, recent developments and further improvements of nuclear resonant scattering spectroscopy that will solve

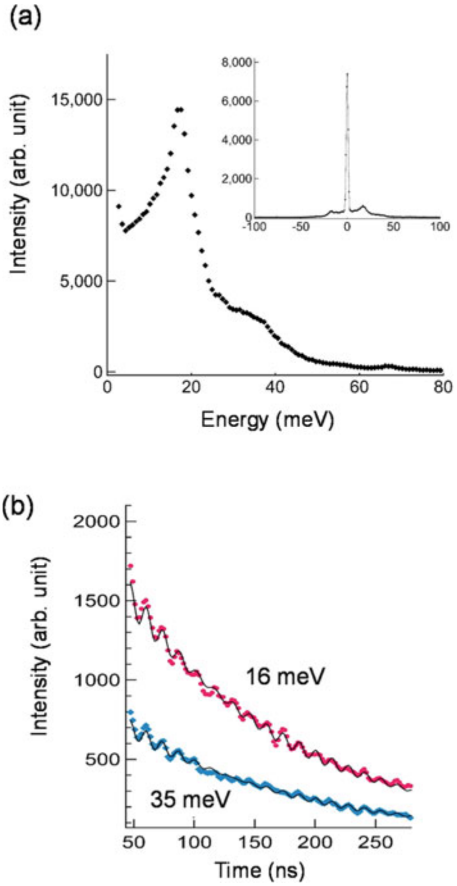

Fig. 2.14 **a** Phonon energy spectrum of nuclear resonant inelastic scattering of ^{57}Fe atoms in Fe_3O_4. Inset is the same spectrum with the elastic peak. **b** Time spectra measured at different incident photon energies referenced from nuclear resonant excitation energy (red circles, 16 meV; blue diamonds, 35 meV). Lines are least-squares fitted spectra with two exponential functions accompanied by sinusoidal quantum beats [6]

problems encountered in electron systems will result in spectroscopy becoming a powerful technique for the study in these areas.

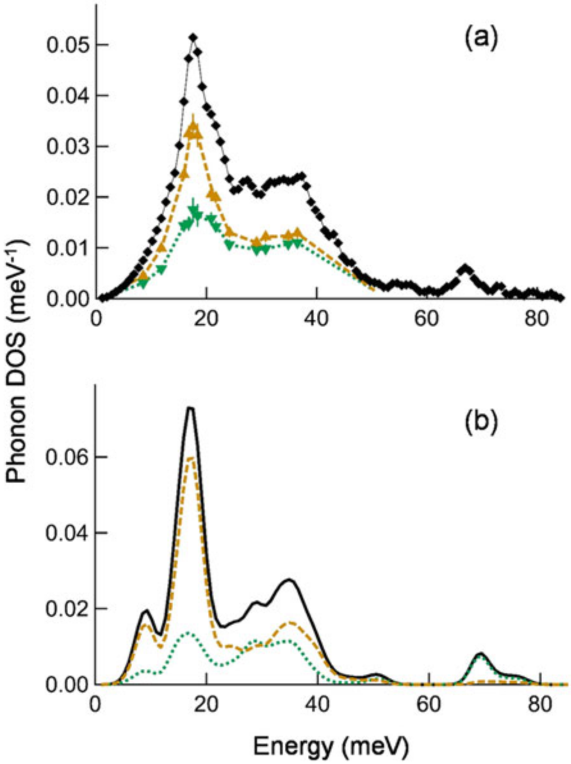

Fig. 2.15 Phonon densities of states (PDOSs) of ^{57}Fe in Fe_3O_4. **a** The PDOSs of Fe are shown by closed black diamonds, and the partial PDOSs of the A and B sites are shown as downward green and upward dark yellow triangles, respectively. Lines are inserted to guide the eye. **b** PDOSs of Fe in the ideal Fe_3O_4 obtained by ab initio calculations. The PDOSs of all Fe are shown as a black line. The calculated partial PDOSs of the A and B sites are shown as dashed green and dashed-and-dotted dark yellow lines, respectively [6]

2.4 Quasielastic Scattering Using Mössbauer γ-Rays

2.4.1 Introduction

Timescale and spatial scale of microscopic density fluctuations in condensed matters are decided by the so-called quasielastic scattering measurements. In Fig. 2.16, we show time and length regions of the fluctuations that can be studied by various quasielastic scattering techniques. In this chapter, we introduce the quasielastic scattering technique using Mössbauer γ-rays as a probe beam. Most of the techniques based on the Mössbauer effect are used to study samples containing nuclear resonant species. In contrast, this technique is used to decide timescale and length scale of the electron density fluctuations in samples that do not contain nuclear resonant species

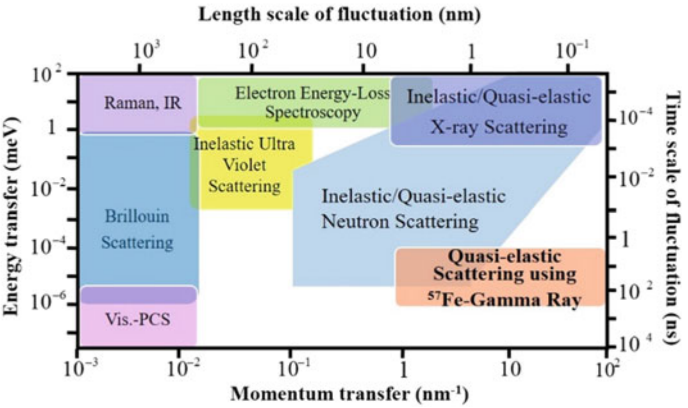

Fig. 2.16 Time and length regions of fluctuations covered by various quasielastic scattering techniques. Quasielastic scattering technique using 14.4-keV γ-rays from ^{57}Fe nuclei covers a unique timescale and length scale

because the Mössbauer effect is used to generate the γ-rays with very high energy resolution and the γ-rays are used for the probe of nonresonant quasielastic scattering study. In Fig. 2.16, we show established time and length regions of the fluctuations that can be studied by quasielastic scattering with 14.4-keV γ-rays from ^{57}Fe nuclei.

This section is composed of the following subsections: In Sect. 2.4.2, basic concepts of quasielastic scattering by nonresonant samples are introduced. In Sect. 2.4.3, the conventional time-domain measurement technique of quasielastic scattering using time-domain interferometry (TDI) with single-line Mössbauer γ-rays is discussed. In Sect. 2.4.4, a finite energy width of incident SR is considered, and the effect on the time spectrum of single-line γ-ray quasielastic scattering is introduced. In Sect. 2.4.5, quasielastic scattering using TDI with multiline Mössbauer γ-rays is described, and its advantage is summarized. In Sect. 2.4.6, results using γ-ray quasielastic scattering are presented. In Sect. 2.4.7, summary and perspective of γ-ray quasielastic scattering are discussed.

2.4.2 Basic Concept of Quasielastic Scattering by Nonresonant Samples

We consider the Rayleigh scattering process of the Mössbauer γ-rays, whose wave vector is $\boldsymbol{k}$, by electrons in a sample, such as liquids. Hereafter, we mainly consider the 14.4-keV Mössbauer γ-rays with 4.66-neV energy width from the first nuclear excited state of ^{57}Fe. In the scattering geometry shown in Fig. 2.17, the γ-rays transfer a momentum $q = |\boldsymbol{k}' - \boldsymbol{k}| = 2k \sin\theta$ to the sample, where $\boldsymbol{k}'$ is the wave vector of the scatted γ-rays and 2θ is the scattering angle. In the elastic Rayleigh scattering case, it follows that $|\boldsymbol{k}| \sim |\boldsymbol{k}'|$. In a simple mono-atom liquid, an electron density

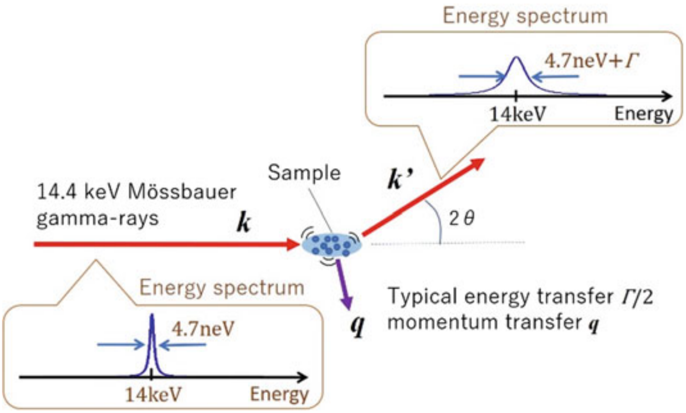

Fig. 2.17 Schematic diagram of quasielastic scattering of Mössbauer γ-rays by a sample

field is written as $\rho(\boldsymbol{r}, t) = \sum_{i=1}^{N} \delta(\boldsymbol{r} - \boldsymbol{r}_i(t))$, where $\boldsymbol{r}$ and t are coordinate and time, respectively; N is a molecular number in the sample; and $\boldsymbol{r}_i$ is a center position of atom i. In the reciprocal $\boldsymbol{q}$ space, the density field is written as $g(\boldsymbol{q}, t) = \int \rho(\boldsymbol{r}, t)\mathrm{e}^{-\mathrm{i}\boldsymbol{q}\cdot\boldsymbol{r}}d\boldsymbol{r}$.

We consider scaler component $q = |\boldsymbol{q}|$, assuming that the sample is isotropic, such as liquids and amorphous solids. When the q dependence of the elastic scattering intensity $I(q)$ is measured, it depends on the static structure factor $S(q)$ as $I(q) = N S(q) \equiv \langle g(q, t)g(-q, t)\rangle$, where $\langle \cdots \rangle$ denotes an ensemble averaging over a long time t. $S(q)$ is related to the space correlation function $G(r) = \langle \rho(r, t)\rho(0, t)\rangle$, which shows the spatial correlation of the electron density with a space r, as $S(q) = \int G(r)\exp(\mathrm{i}qr)dr$.

In the presence of atomic/molecular motions in a sample, the energy of the γ-rays is transferred to the sample and vise visa. We consider the microscopic dynamics in timescales between nanosecond and microsecond. Here, we consider quasielastic scattering process, which broadens the width of the energy spectrum, as shown in Fig. 2.17. The energy transfer is very small (approximately 10^{-9} eV) compared to the γ-ray energy (approximately 10 keV). Therefore, we can still assume that $|\boldsymbol{k}| \sim |\boldsymbol{k}'|$.

When we analyze the energy of the scattered γ-rays at q by standard Mössbauer absorption spectroscopy, we can observe that $I(q, E) = NS(q, E)$, where $S(q, E)$ is called the dynamics structure factor. $S(q, E)$ is related to the time and space correlation function $G(r, t)$: $S(q, E) = \int G(r, t)\exp[\mathrm{i}(qr - tE/\hbar)]dtdr$. Here, $\hbar$ is the reduced Planck constant. Inelastic/quasi-elastic X-ray and neutron scattering measures $S(q, E)$. Similarly, in the time domain, the corresponding $S(q, t) = \int S(q, E)\exp(\mathrm{i}tE/\hbar)dE$ is measured by neutron spin echo spectroscopy. Both $S(q, E)$ and $S(q, t)$ show equivalent information on microscopic time–space picture $G(r, t)$.

Quasielastic scattering experiments using Mössbauer γ-rays from RI sources have been performed soon after the discovery of the Mössbauer effect in1960s [110]. The method is called as RSMR [111]. However, because γ-rays from an RI source do not have enough brilliance as a parallel beam required for quasielastic scattering experiments, the method requires much measuring time (e.g., weeks). In this section, we call the quasielastic scattering spectroscopy using the γ-rays as quasielastic γ-ray scattering (QEGS) spectroscopy. Recently, high-brilliance SR is available and widely used for Mössbauer spectroscopy [112]. Using SR, QEGS was demonstrated by some techniques. First, QEGS using ^{57}Fe-nuclear Bragg monochromator, which measures $S(q, E)$, was attempted and demonstrated [113, 114]. Then, QEGS using TDI of ^{57}Fe γ-rays, which observes $S(q, t)$, was demonstrated [115]. These methods allowed a much quicker measurement of the atomic/molecular dynamics than the RSMR method owing to high brilliance and directivity of the SR sources and technological development of the high-resolution monochromator [116] and APD detector [24].

2.4.3 *Time-Domain Measurement of Quasielastic Scattering of Mössbauer Gamma Rays Using Synchrotron Radiation*

In this subsection, we introduce quasielastic scattering method using TDI with single-line Mössbauer γ-rays.

In Sect. 2.4.3.1, we introduce NFS experiment with single-line γ-ray emitters. This experiment corresponds to the QEGS experiment without a sample. In Sect. 2.4.3.2, the corresponding QEGS using TDI with single-line γ-rays is considered. In Sect. 2.4.3.3, we introduce an interpretation of the time spectrum from space-time diagram. In Sect. 2.4.3.4, we discuss the selectivity of nuclear species for TDI.

2.4.3.1 Introduction of Nuclear Forward Scattering Using Time-Domain Interferometry Setup of Single-Line Mössbauer Gamma Rays

Before the discussion of the QEGS experiment, it is valuable to consider corresponding NFS with two single-line γ-ray emitters because the NFS experiment corresponds to QEGS experiment without a sample and is a basis of QEGS using TDI. The NFS experimental setup is shown in the upper figure of Fig. 2.18a. The incident SR is introduced to two identical materials containing ^{57}Fe with single-line nuclear excitation profile. After transmitting them, the time spectrum of the SR and γ-rays from the materials are detected by a detector, such as an APD detector, with a time resolution of ~1 ns. Hereafter, we call the upstream and downstream emitters as γ-ray emitters 1 and 2, respectively. Here, we assume that emitter 1 is driven with a constant velocity v in the direction of the incident SR wave vector $\boldsymbol{k}$ to change the γ-ray energy from that of downstream emitter 2 by the Doppler effect. The relation between applied

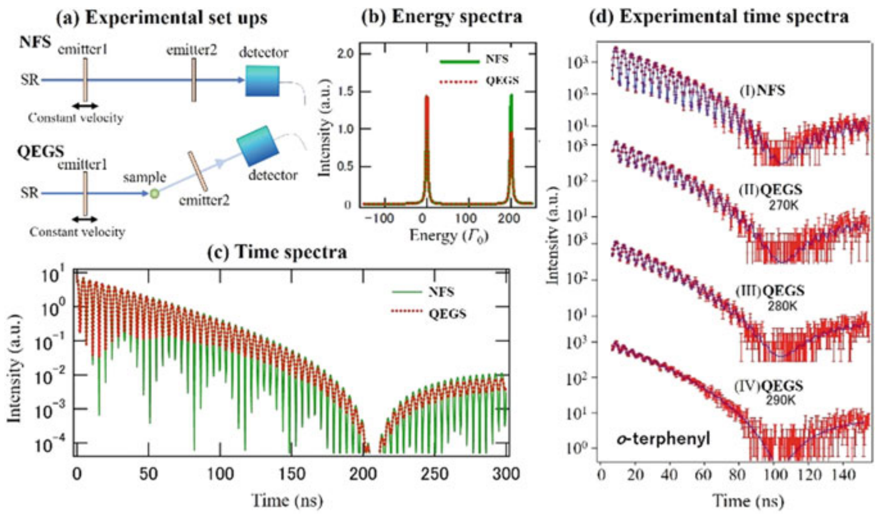

Fig. 2.18 Experimental setups and spectra of NFS and QEGS using the single-line TDI. **a** Experimental setups, **b** theoretical energy spectra, **c** theoretical time spectra, and **d** experimentally obtained time spectra using (I) NFS and QEGS studies on *o*-terphenyl at (II) 270 K, (III) 280 K, and (IV) 290 K. In panel **d**, points represent experimentally obtained counts of γ-rays, and vertical bars represent the statistic errors (standard deviations). The lines are fitting curves using eq. (2.3)

velocity v and the energy shift of γ-rays δE is expressed as $\delta E = E_\gamma v/c$, where c is the speed of light and E_γ is the energy of the γ-rays. For example, for the case of v~10 mm/s, which is easily realized by the velocity transducer produced by e.g. the WissEl GmbH, we obtain $\delta E \sim 100\Gamma_0$, which is much larger than the natural energy width of γ-rays, Γ_0. Simultaneously, this δE value is much smaller than the energy width of the incident SR typically approximately meV (~$10^6\Gamma_0$). Therefore, the nuclear resonant excitation process occurs in the same condition in two emitters. We can detect the interference of the γ-rays in the directive forward scattering component. [14]

In such a case, we consider the energy spectrum of γ-rays from two emitters at the forward detector position. The spectrum shows two peaks sufficiently separated, as shown in Fig. 2.18b. Here, the horizontal axis is a relative energy to the γ-ray energy from emitter 2 scaled by the energy unit of Γ_0. On the NFS time spectrum, we see a beating pattern called a quantum beat, which originates from the interference of γ-rays with different energies from two emitters, as shown in Fig. 2.18c.

First, we describe the property of the incident SR. The amplitude of the incident SR electric field SR in the angular frequency ω domain is expressed as $\hat{E}_0(\omega)$. The incident SR is usually monochromatized around the nuclear excitation energy to reduce the unused radiation for preventing system damage. In such a case, the bandwidth ΔE of $\left|\hat{E}_0(\omega)\right|^2$ is in the order of meV. The phase of each frequency component is assumed to be the same [117].

We write the electric field amplitude of the incident SR in the time t domain as $E_0(t)$, which is related to $\hat{E}_0(\omega)$ by Fourier transformation. The time response functions of emitters 1 and 2 are defined to be as follows [117, 118]:

$$\begin{aligned} &R_1(t) = \delta(t) + G(t)\mathrm{e}^{\mathrm{i}\delta Et/\hbar} \\ &\text{and} \\ &R_2(t) = \delta(t) + G(t), \end{aligned} \tag{2.13}$$

where $\delta(t)$ represents a transmission part without nuclear excitation process and the second term including $G(t)$ represents the nuclear excitation and de-excitation processes with the Mössbauer effect. The energy shift of γ-rays from the upstream emitter is considered by a term that includes the corresponding angular frequency $\delta E/\hbar$. Here, we ignored a transmittance factor because it does not affect the shape of the time spectrum. When the energy shift is sufficiently large ($\delta E \gg \Gamma_0$), unfavorable radiative coupling (RC; photons experience nuclear excitation processes in both emitters) can be neglected [119]. We consider the $\delta E \gg \Gamma_0$ case in the following discussion.

The electric field amplitude after emitter 1 is written as $R_1(t) \otimes E_0(t)$, where $\otimes$ denotes the convolution integral [117, 119]. After transmitting emitter 2, the electric field amplitude is written as $R_2(t) \otimes \{R_1(t) \otimes E_0(t)\}$. When $\left|\hat{E}_0(\omega)\right|^2$ shows a finite bandwidth $\Delta E/\hbar$, $|E_0(t)|^2$ also shows a finite width $\Delta T \sim \mathrm{h}/\Delta E$. In the timescale of ΔT, the incident SR partly shows time coherence. ΔT is much smaller than the nuclear response as shown below. Therefore, we assume $E_0(t) \propto \delta(t)$. Here, the electric field amplitude $E_{tot}(t)$ at the detector position can be written as

$$E_{tot}(t) \propto \int_0^\infty R_1(t')R_2(t-t')\mathrm{d}t' \approx \delta(t) + G(t)\left(1 + \mathrm{e}^{i\delta Et/\hbar}\right). \tag{2.14}$$

Here, the origin of the time is the detection time of the SR pulse. The electric field amplitude of γ-rays $E(t)$ is written as $E(t) \propto G(t)\left(1 + \mathrm{e}^{i\delta Et/\hbar}\right)$. The intensity is given by

$$\begin{aligned} I(t) &= |E(t)|^2 \\ &= 2|G(t)|^2[1 + \cos(\delta Et/\hbar)]. \end{aligned} \tag{2.15}$$

Here, the factor $|G(t)|^2$ represents the NFS time spectrum from one emitter. In a thin limit of the emitter thickness, it follows that $|G(t)|^2 \propto \mathrm{e}^{-t/\tau_0}$, where τ_0 is the lifetime of the nuclear excited state. Otherwise, $|G(t)|^2$ shows more complex time dependence known as a dynamical beat [120]. In the ^{57}Fe case, τ_0 is ~141 ns. A factor $1 + \cos(\delta Et/\hbar)$ represents a quantum beat modifying $|G(t)|^2$.

Here, the velocity transducer used to drive emitter 1 brings a constant velocity with positive and negative sign, alternatively. Note that the sign of the velocity of the driven emitter 1 does not affect the obtained time spectrum $I(t)$, because only an absolute value of the energy difference between γ-rays from the two emitters is important for the beating pattern on the time spectrum owing to the factor $\cos(\delta Et/\hbar) = \cos(-\delta Et/\hbar)$ in eq. (2.15). In actual experiments, we do not detect signals in the period, where the velocity is not constant owing to the change of sign of the velocity. We also note that following time distributions have to be treated as an incoherent broadening of the time spectrum: (1) the time resolution of the detector (in this study ~1 ns) and (2) the distribution of the arrival time of SR owing to the spatial distribution of the electrons in one bunch (approximately 50 ps (FWHM) in BL09XU of SPring-8). As an experimental time spectrum, we obtain $\bar{I}_{\mathrm{exp}}(t) = I(t) \otimes D(t) + B$, where $D(t)$ is the total incoherent distribution function and B is a background constant noise.

2.4.3.2 Quasielastic Scattering Using Time-Domain Interferometry of Single-Line Mössbauer Gamma Rays

Next, we consider QEGS experimental setup shown in the lower figure of Fig. 2.18a and derive the expression of the QEGS time spectrum. Here, we introduce the sample response function $g(q,t)$. It cannot be immediately assumed that $E_0(t) \propto \delta(t)$ because we do not know the timescale of the sample response [121]. Only the case that the sample shows longer time response than ΔT that we can assume $E_0(t) \propto \delta(t)$. In this subsection, we assume this specific case of $E_0(t) \propto \delta(t)$ because it makes the discussion simpler and instructive. The effect of the finite time width of the incident SR on the QEGS time spectrum is discussed in Sect. 2.4.4 based on the discussion of this subsection.

The electric field amplitude after emitter 1 is $R_1(t) \otimes E_0(t)$. We define t_s as a time when the Rayleigh scattering process of the prompt SR pulse occurs in the sample. The sample response generally depends on both t_s and t. Conversely, the nuclear response is independent of t_s [119, 122]. The electric field amplitude after scattering by the sample is written as $g(q, t_s + t)E_A(t)$, where we used the time response function of the sample $g(q, t_s + t)$ defined in Sect. 2.4.2 [115]. After transmitting emitter 2, the total electric field amplitude $E_{tot}(q, t_s + t)$ at the angle corresponding to q is

$$E_{tot}(q, t_s + t) \propto R_2(t) \otimes \{g(q, t_s + t)[R_1(t) \otimes E_0(t)]\}. \tag{2.16}$$

By assuming $E_0(t) \propto \delta(t)$, $E_{tot}(q, t_s + t)$ is written as

$$E_{tot}(q, t_s + t) \propto \int_0^\infty R_1(t')g(q, t_s + t')R_2(t - t')\mathrm{d}t'. \tag{2.17}$$

Neglecting the RC effect, we obtain the electric field amplitude of γ-rays $E(q, t_s + t)$ as

$$E(q, t_s + t) \propto g(q, t_s + t)G(t)\mathrm{e}^{\mathrm{i}\delta Et/\hbar} + g(q, t_s)G(t). \tag{2.18}$$

Similarly, to the NFS case, the theoretical equation of the γ-ray time spectrum is written as $I\left(q, t_s + t\right) \propto \left|G(t)\right|^2\left[\left|g\left(q, t_s + t\right)\right|^2 + \left|g\left(q, t_s\right)\right|^2 + g\left(q, t_s + t\right)g^*\left(q, t_s\right)\mathrm{e}^{\mathrm{i}\delta Et/\hbar} + g^*\left(q, t_s + t\right)g\left(q, t_s\right)\mathrm{e}^{-\mathrm{i}\delta Et/\hbar}\right]$. The experimentally observed $\bar{I}(q, t)$ is obtained by averaging $I(q, t_s + t)$ by t_s over a long measurement time as

$$\begin{aligned}\bar{I}(q, t) \propto |G(t)|^2\big[&\left\langle|g(q, t_s + t)|^2\right\rangle + \left\langle|g(q, t_s)|^2\right\rangle \\ &+ \left\langle g(q, t_s + t)g^*(q, t_s)\right\rangle \mathrm{e}^{\mathrm{i}\delta Et/\hbar} + \left\langle g^*(q, t_s + t)g(q, t_s)\right\rangle \mathrm{e}^{-\mathrm{i}\delta Et/\hbar}\big]\end{aligned} \tag{2.19}$$

where $\langle\cdots\rangle$ indicates averaging by t_s over a long measurement time. It follows that $S(q, 0) = \left\langle|g(q, t_s + t)|^2\right\rangle = \left\langle|g(q, t_s)|^2\right\rangle$. In classic mechanical cases, it follows that $S(q, t) = \langle g^*(q, t_s + t)g(q, t_s)\rangle = \langle g(q, t_s + t)g^*(q, t_s)\rangle$ suggesting $S(q, t)$ can be treated as a real number [115, 119, 122, 123]. We define $S'(q, t)$ as the intermediate scattering function normalized by $S(q, 0)$ as

$$S'(q, t) = \langle g(q, t_s + t)g(q, t_s)\rangle / \left\langle|g(q, t_s + t)|^2\right\rangle, \tag{2.20}$$

we obtain

$$\bar{I}(q, t) \propto |G(t)|^2 S(q)\left[1 + S'(q, t)\cos(\delta Et/\hbar)\right]. \tag{2.21}$$

When a single exponential relaxation is assumed for $S'(q, t)$, we can write $S'(q, t) \propto \exp\{-t/\tau\}$, where τ is a relaxation time. Often, there is an intrinsic relaxation in $S'(q, t)$ even when standard samples with no detectable dynamics are measured [115]. To express it, we introduce a relaxation function $F^{\mathrm{int}}(t)$. By using this factor, the time spectrum is given by

$$\bar{I}(q, t) \propto |G(t)|^2\left[1 + F^{\mathrm{int}}(t)S'(q, t)\cos(\delta Et/\hbar)\right]. \tag{2.22}$$

The measured time spectrum $\bar{I}_{\exp}(q, t)$ is written as $\bar{I}_{\exp}(q, t) = \bar{I}(q, t) \otimes D(t) + B$ as described in Sect. 2.4.3.1.

We calculated NFS and QEGS time spectra, as shown in Fig. 2.18c, where we used the following conditions: the effective thickness of each emitter $T_{\mathrm{e}} = 10$, $v = 20$ mm/s, and $\tau = 0.5\tau_0$. The corresponding γ-ray energy spectra are shown in Fig. 2.18b. The figure shows that the time-spectrum shape changes, reflecting dynamics as the disappearance of the quantum beat.

In Fig. 2.18d, experimentally obtained time spectra by (I) NFS and QEGS studies on *o*-terphenyl at (II) 270 K, (III) 280 K, and (IV) 290 K are shown. It can be confirmed that the quantum beat disappears by heating the sample. Least squares fittings using eq. (2.22) were successfully performed considering the time resolution $D(t)$ and background. The obtained relaxation time was confirmed to be consistent with previous results [124].

2.4.3.3 Interpretation of Time Spectrum of Quasielastic Scattering from Space–Time Diagram

We consider why the interference of γ-rays disappears with a time using the space–time diagram of photon paths for QEGS using TDI. We show the diagram in Fig. 2.19. We took the position of the photons on the beam path as a bottom axis of the figure. The vertical axis represents the time t_s. This figure shows that paths I and II constitute an interferometer, in which one arm of the interferometer is in the time domain and the other arm is in the space domain, compared to the usual interferometers with two arms in the space domain [112]. This is the reason why this method is named the "time-domain interferometry." We consider paths I and II of the γ-rays detected at delayed time compared to the SR pulse in the diagram. In Fig. 2.19, filled/empty circle symbols on the beam path express nuclear excitation/de-excitation events in emitters, and the star symbols show the Rayleigh scattering event by the sample. At the filled circle points, nuclear excitation event occurs as if the γ-rays are trapped until the excited nuclei decay. We do not consider the radiative coupling path that γ-rays experience the nuclear excitation event in both emitters because the excitation energies in the two emitters are sufficiently different from each other.

As we can see in eq. (2.21), the amplitude of the beating pattern of the time spectra decays following $S'(q, t)$. This suggests that time coherence of γ-ray photons from the two emitters decreases with time due to diffusion in samples. In other words, the time spectrum shape changes with time from the time spectrum shape calculated from the coherent sum of the electric fields from both emitters to the time spectrum shape calculated from the incoherent sum of the electric fields from each emitter due to the loss of the coherency of γ-rays. This explanation suggests that the measurement efficiency of QEGS using TDI strongly depends on the degree of difference between the coherent and incoherent time spectra, and the efficiency of QEGS using TDI can be improved by selecting the emitters.

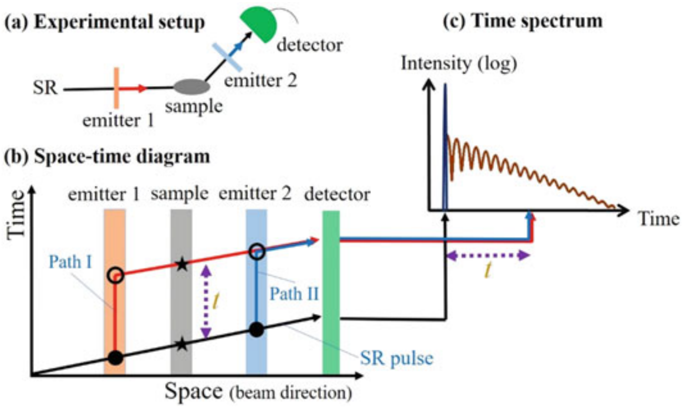

Fig. 2.19 **a** Experimental setup, **b** space–time diagram, and **c** time spectrum of the conventional TDI for QEGS

Table 2.2 Examples of Mössbauer isotopes [112]

Isotopes	Gamma ray energy (keV)	Gamma ray energy width (neV)	Nuclear resonant cross section (barn)
^{57}Fe*	14.4125	4.66	2464.0
^{67}Zn	93.312	0.0498	50.0
^{119}Sn	23.871	25.70	1380.5
^{149}Sm	22.494	64.08	120.1
^{151}Eu*	21.532	47.03	242.6
^{181}Ta	6.238	0.0754	1099.2

*Symbol indicates nuclear species already demonstrated to be available for the QEGS study

2.4.3.4 Selectivity of Isotopes for Quasielastic Scattering Experiment Using Time-Domain Interferometry

In quasielastic scattering measurements using γ-rays, the time (energy) and space (momentum) regions of the measurement depend on the characteristics (lifetime and excitation energy) of the nuclear resonance of isotopes used and other experimental conditions. In QEGS experiments using TDI, the short limit of the accessible time range depends on, for example, the time resolution of the detector, while the long limit depends on the lifetime of the nuclear excited state. The γ-ray energy, energy width, and nuclear resonant cross section for some Mössbauer isotopes are shown in Table 2.2. So far, QEGS experiments using TDI with ^{57}Fe and ^{151}Eu were demonstrated [125].

2.4.4 *Effect of Energy Width of Incident Synchrotron Radiation*

Here, we consider the general case that the time profile of the incident SR cannot be treated as a delta function [121]. When the high-resolution monochromator with meV energy resolution is used for the monochromatization of incident beam, the corresponding coherent time width is sub-picoseconds, In the timescale, usual condensed matter shows vibration motions. Therefore, normally, the incident SR cannot be treated as a delta function; instead, the sample response in the timescale must be considered by the exact calculation of interaction between the electric field and the sample.

We define a period δT_{12} for quantum beats caused by the interference between γ-rays from emitters 1 and 2. In the general case, the energy spectrum of the γ-rays from each emitter may show multi-peaks. Therefore, there are various quantum beats with various periods. For any quantum beats, we assume $\tau_0 \gg \delta T_{12} \gg \Delta T$. In such a case, the RC effect is negligible. From eq. (2.16), the electric field amplitude of the γ-rays is written as

$$E(q, t_s + t) = \int\limits_{-\infty}^{\infty} dt' \left[g(q, t_s + t) G_1\left(t - t'\right) E_0\left(t'\right) + G_2\left(t - t'\right) g\left(q, t_s + t'\right) E_0\left(t'\right) \right]. \tag{2.23}$$

The first and second terms of eq. (2.23) describe the electric field amplitudes of the γ-rays passing paths I and II in Fig. 2.19, respectively.

In this subsection, we consider the experimental setup with single-line γ-ray emitters shown in Fig. 2.18a. Here, we assume $G_1(t) = G_2(t) \mathrm{e}^{i\delta Et/\hbar}$ and $G_2(t) = G(t)$. The electric field amplitude of the γ-rays is as follows:

$$\begin{aligned} E(q, t_s + t) = \int\limits_{-\infty}^{\infty} & dt' g(q, t_s + t) G\left(t - t'\right) \mathrm{e}^{i\delta E\left(t - t'\right)\hbar} E_0\left(t'\right) \\ & + G\left(t - t'\right) g\left(q, t_s + t'\right) E_0\left(t'\right). \end{aligned} \tag{2.24}$$

The time variation of $|G(t)|$ is much slower than that of $|E_0(t)|$ from the relation $\tau_0 \gg \delta T_{12} \gg \Delta T$. Therefore, the first term in eq. (2.24) follows that $g(q, t_s + t) \int\limits_{-\infty}^{\infty} dt' G\left(t - t'\right) \mathrm{e}^{i\delta E\left(t - t'\right)\hbar} E_0\left(t'\right) \cong g(q, t_s + t) G(t) \mathrm{e}^{i\delta Et/\hbar} \int\limits_{-\infty}^{\infty} dt' E_0\left(t'\right)$. Similarly, the second term follows that $\int\limits_{-\infty}^{\infty} dt' G\left(t - t'\right) g\left(q, t_s + t'\right) E_0\left(t'\right) \cong G(t) \int\limits_{-\infty}^{\infty} dt' g\left(q, t_s + t'\right) E_0\left(t'\right)$. Here, we define $g_c(q, t_s)$ as $g_c(q, t_s) \equiv \int\limits_{-\infty}^{\infty} dt' g\left(q, t_s + t'\right) E_0\left(t'\right) / \int\limits_{-\infty}^{\infty} dt' E_0\left(t'\right)$. In case of $E_0(t) = \delta(t)$, it follows that $g_c(q, t_s) = g(q, t_s)$. Using g_c, eq. (2.24) can be written as

$$E(q, t_s + t) \cong \hat{E}_0(0) G(t) \left[g(q, t_s + t) \mathrm{e}^{i\delta Et/\hbar} + g_c(q, t_s) \right], \tag{2.25}$$

where we used the general relation $\int\limits_{-\infty}^{\infty} dt' E_0\left(t'\right) = \hat{E}_0(0) \equiv \hat{E}_0(\omega = 0)$. Here, $\hat{E}_0(\omega)$ is the angular frequency-domain representation of $E_0(t)$.

Here, we consider the meaning of $g_c(q, t_s)$, which is an integration of the product of $g\left(q, t_s + t'\right)$ and $E_0\left(t'\right)$ by t'. We show examples of paths I and II of the γ-rays detected at t with an incident time $t' = 0$ (long dashed line) and $t' \neq 0$ (short dashed line) in the time–space diagrams of Figs. 2.20a and b, respectively. Gamma rays with different incident times t' interfere at the detector owing to the finite coherent width of $E_0(t)$ in both γ-ray paths I and II. The integration in $g_c(q, t_s)$ originates from a characteristic of path II: γ-rays scattered by the sample at various times $t_s + t'$ ($\left|t'\right| \lesssim \Delta T$) interfere with each other at the detector position at t. Alternatively, in path I, the γ-rays scattered by the sample at unique time $t_s + t$ interfere with each other at the detector position at t. Therefore, the γ-rays passing path I are not affected by the time width ΔT of the incident radiation. This is the interpretation of eq. (2.25).

From eq. (2.16), we obtain the detected γ-ray intensity:

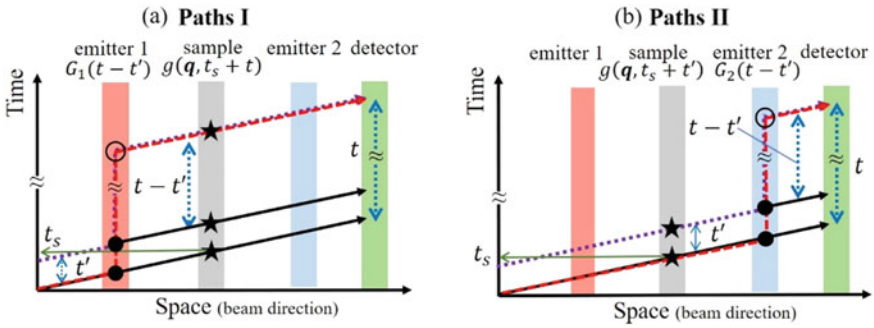

Fig. 2.20 Examples of paths **a** I and **b** II of the γ-rays detected at t with an incident time $t'=0$ (long dashed line) and $t'\neq 0$ (short dashed line) for the time–space diagrams

$$I(q,t_s+t)\propto|G(t)|^2\Big[|g(q,t_s+t)|^2+|g_c(q,t_s)|^2 \\ +\Big\{g^*(q,t_s+t)g_c(q,t_s)+g(q,t_s+t)g_c^*(q,t_s)\Big\}\cos(\delta Et/\hbar). \tag{2.26}$$

The experimental spectrum $\bar{I}(q,t)$ is obtained by averaging $I(q,t_s+t)$ by t_s over a long measurement time. As we discussed in Sect. 2.4.3.2, it follows $S(q,t)=\langle g^*(q,t_s+t)g(q,t_s)\rangle=\langle g(q,t_s+t)g^*(q,t_s)\rangle$. We define correlation functions $S_{cc}(q,t)$ and $S_\mathrm{c}(q,t)$ as $\big\langle g_c(q,t_s+t)g_\mathrm{c}^*(q,t_s)\big\rangle$ and $\big\langle g(q,t_s+t)g_\mathrm{c}^*(q,t_s)\big\rangle$ averaged by t_s, respectively. It can be assumed that $S_{cc}(q,t)$ is also a real number. Using these values, the observed time-averaging intensity $\bar{I}(q,t)$ can be written as

$$\bar{I}(q,t)\propto|G(t)|^2\Big\{S(q,0)+S_{cc}(q,0)+\big[S_c(q,t)+S_\mathrm{c}^*(q,t)\big]\cos(\delta Et/\hbar)\Big\}. \tag{2.27}$$

Here, $S_c(q,t)$ is written as

$$S_c(q,t)=\big\langle g^*(q,t_s+t)g_c(q,t_s)\big\rangle=\frac{1}{\hat{E}_0(0)}\int_{-\infty}^{\infty}dt'E_0\big(t'\big)S\big(q,t-t'\big). \tag{2.28}$$

The γ-ray time spectra are observed in the timescale much longer than ΔT. In the timescale, it can be assumed that $\int_{-\infty}^{\infty}dt'E_0\big(t'\big)S\big(q,t-t'\big)\cong S(q,t)\int_{-\infty}^{\infty}dt'E_0\big(t'\big)$ because, in the measurement time window, the variation of $S(q,t)$ in the timescale ΔT is usually negligible. Therefore, it follows that $S_c(q,t)\cong S(q,t)\int_{-\infty}^{\infty}dt'E_0\big(t'\big)/\hat{E}_0(0)\cong S(q,t)$ and $S_c(q,t)\cong S_\mathrm{c}^*(q,t)$. $\bar{I}(q,t)$ is written as follows:

$$\bar{I}(q,t)\propto|G(t)|^2[S(q,0)+S_{cc}(q,0)+2S(q,t)\cos(\delta Et/\hbar)](\mathrm{at}t\gg\Delta T). \tag{2.29}$$

The experimental time spectrum is written as $\bar{I}_{\mathrm{exp}}(q,t) = \bar{I}(q,t) \otimes D + B$ discussed above.

From the definition of $S_{cc}(q,t)$, it follows that

$$S_{cc}(q,t) = \frac{1}{\left|\hat{E}_0(0)\right|^2} \int_{-\infty}^{\infty} \int_{-\infty}^{\infty} dt' dt'' E_0(t') E_0^*(t'') \langle g(q, t_s + t') g^*(q, t_s + t + t'') \rangle$$
$$\equiv \int_{-\infty}^{\infty} dt_d I_0(t_d) S(q, t + t_d) \tag{2.30}$$

where $t_d \equiv t'' - t'$. We define $I_0(t_d) \equiv \int_{-\infty}^{\infty} dt' E_0^*(t') E_0(t_d + t') / \left|\hat{E}_0(0)\right|^2$. The typical timescale of the decay of $I_0(t_d)$ is ΔT as defined in Sect. 2.4.3.1. We show a schematic diagram as example of $S_{cc}^{'}(q,t)$ in Fig. 2.21. When $t \gg \Delta T$, it follows that $S_{cc}(q,t) \sim S(q,t)$ by neglecting the time variation of $S(q,t)$ in the timescale ΔT, as assumed in the above discussion of $S_c(q,t)$. Conversely, when $t = 0 \ll \Delta T$, we obtain $S_{cc}(q,0) = \int_{-\infty}^{\infty} dt_d I_0(t_d) S(q, t_d)$, suggesting that $S_{cc}(q,0) \sim S(q, \Delta T)$. We define the $S_{cc}(q,0)$ value as $S_{cc}(q,0) \equiv f_{\Delta E}(q)$, as shown in Fig. 2.21. When ΔE is sufficiently large and $f_{\Delta E}(q) = 1$ can be assumed, we obtain $\bar{I}(q,t) \propto |G(t)|^2 \left[1 + S'(q,t)\cos(\delta E t/\hbar)\right]$, which is equivalent to eq. (2.21).

$S'(q,t)$ generally shows a form with vibrations and multistep relaxations, which spread over very wide time ranges. See Fig. 2.21 for an example of $S'(q,t)$ and its relation to $S_{cc}^{'}(q,t)$. Here, $\bar{I}(q,t)$ is usually fitted by assuming a relaxation function $F(q,t)$, which represents relaxations of $S'(q,t)$ in the time window of the measurement approximately the timescale of τ_0. In Fig. 2.21, we show an example of $F(q,t)$. Here, we define $f_{\Gamma_0}(q) \equiv \lim_{t \to 0} F(q,t)$. $f_{\Gamma_0}(q)$ is a plateau value of $S'(q,t)$ decided by the fitting of the time spectrum, as shown in Fig. 2.21. Both $f_{\Delta E}(q)$ and $f_{\Gamma_0}(q)$ give unique information on microscopic dynamics. Hence, special attention must be given for these definitions.

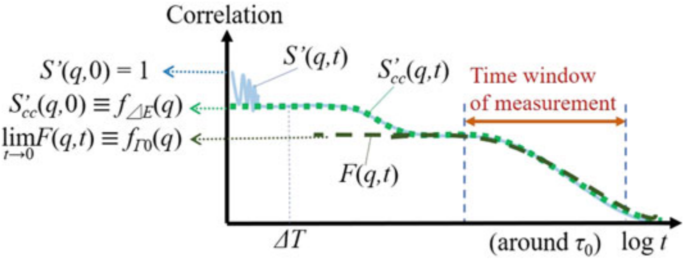

Fig. 2.21 Example of the intermediate scattering function normalized by the static structure factor $S'(q,t)$ with its relation to $S'_{cc}(q,t)$ and assumed $F(q,t)$

Here, we show that neither $f_{\Gamma_0}(q)$ nor $f_{\Delta E}(q)$ cannot be determined by the conventional single-line TDI in the case of finite ΔE width of approximately several meV using a high-resolution monochromator. From eq. (2.29), we obtain

$$\bar{I}(q,t) \propto |G(t)|^2 \big\{1 + 2S'(q,t)/[1 + f_{\Delta E}(q)]\cos(\delta E t/\hbar)\big\}. \tag{2.31}$$

In this equation, the cosine term has an additional factor $2/[1 + f_{\Delta E}(q)]$ compared to eq. (2.21). When this expression is used for the fitting, a function $F'(q,t)$ is assumed for $2S'(q,t)/[1 + f_{\Delta E}(q)]$. Using $F(q,t)$, which represents the form of $S'(q,t)$ in the time window of the measurement, $F'(q,t)$ can be expressed as $F'(q,t) = 2F(q,t)/[1 + f_{\Delta E}(q)]$. It follows that $\lim_{t\to 0} F'(q,t) = 2\lim_{t\to 0} F(q,t)/[1 + f_{\Delta E}(q)] = 2f_{\Gamma_0}(q)/[1 + f_{\Delta E}(q)]$. This equation suggests that both free fitting parameters $f_{\Gamma_0}(q)$ and $f_{\Delta E}(q)$ relate to $\lim_{t\to 0} F'(q,t)$. Therefore, in principle, neither $f_{\Delta E}(q)$ nor $f_{\Gamma_0}(q)$ can be determined by the single-line TDI when an identical pair of emitters are used in the incident SR condition with meV energy width. The conventional TDI suffers this uncertainty of the physical meaning of $\lim_{t\to 0} F'(q,t)$.

In contrast, for the case of a multiline emitter case with $|G_1(t)|^2 \neq |G_2(t)|^2$, both $f_{\Delta E}(q)$ and $f_{\Gamma_0}(q)$ can be determined based on the difference between $|G_1(t)|^2$ and $|G_2(t)|^2$ as we discuss in Sect. 2.4.5 [121].

2.4.5 Time-Domain Interferometry Using Multiline Mössbauer Gamma Rays

In the case where multiline γ-rays with $|G_1(t)|^2 \neq |G_2(t)|^2$ are used for TDI, the intensity of the γ-rays from eq. (2.23) is written as

$$\begin{aligned} I(q, t_s + t) \propto\ & |G_1(t)|^2 |g(q, t_s + t)|^2 + |G_2(t)|^2 |g_c(q, t_s)|^2 \\ & + G_1^*(t) G_2(t) g^*(q, t_s + t) g_c(q, t_s) \\ & + G_1(t) G_2^*(t) g(q, t_s + t) g_c^*(q, t_s). \end{aligned} \tag{2.32}$$

Similarly, in Sect. 2.4.4, the observed time-averaging intensity $\bar{I}(q,t)$ can be written as

$$\begin{aligned} \bar{I}(q,t) \propto\ & S(q,0)|G_1(t)|^2 + S_{cc}(q,0)|G_2(t)|^2 \\ & + S(q,t)\big[G_1^*(t)G_2(t) + G_2^*(t)G_1(t)\big](\text{at}\, t \gg \Delta T). \end{aligned} \tag{2.33}$$

Using $S'(q,t)$ and $f_{\Delta E}(q)$, $\bar{I}(q,t)$ can be rewritten as

$$\begin{aligned} \bar{I}(q,t) \propto\ & \big[1 - S'(q,t)\big]\big[|G_1(t)|^2 + |G_2(t)|^2\big] + S'(q,t)|G_1(t) + G_2(t)|^2 \\ & - [1 - f_{\Delta E}(q)]|G_2(t)|^2 \quad (\text{at}\, t \gg \Delta T). \end{aligned} \tag{2.34}$$

The experimental time spectrum is $\bar{I}_{\mathrm{exp}}(q,t) = \bar{I}(q,t) \otimes D(t) + B$. The γ-rays from α-iron foils show energy spectra with a multiline structure. In Fig. 2.22a, we show an example of the experimental setup using α-iron foils as emitters 1 and 2. To satisfy the condition $|G_1(t)|^2 \neq |G_2(t)|^2$, an external magnetic field $\boldsymbol{H}$ is applied to the foils different from each other to selectively allow the excitation between energy levels split by the hyperfine interaction: The direction is horizontal to the electric field of the incident radiation and a direction $\boldsymbol{H} \perp \boldsymbol{k}$ for emitter 1. For emitter 2, the direction is vertical to the electric field of the incident radiation an $\boldsymbol{H} \perp \boldsymbol{k}'$ [126]. The energy spectra of γ-rays in Fig. 2.22b are shown for the case without relaxation and with a relaxation of $\tau = 100\,\mathrm{ns}$. Here, $\delta E_{12} = \mathrm{h}/\delta T_{12} \sim 20\Gamma_0 \gg \Gamma_0$. When $20\Gamma_0 \gg \Gamma$, the RC effect is negligible. The corresponding time spectra of γ-rays are shown in Fig. 2.22c. The shape of the time spectrum changes following the decay of $S'(q,t)$.

In Fig. 2.22d, the experimentally obtained time spectra by QEGS studies on glycerol are shown. The QEGS spectra were obtained (I) at 40 K at 14 nm^{-1}, (II) at 237.5 K at 14 nm^{-1}, and at 237.5 K at 31 nm^{-1}. We note that the experimental condition is different from the theoretical one. Least squares fitting using eq. (2.34) was successfully performed, and the obtained relaxation time was confirmed to be consistent with previous results [121]. It was shown that the measurement efficiency of the multiline TDI system is much higher than the single-line system one [121, 126, 127].

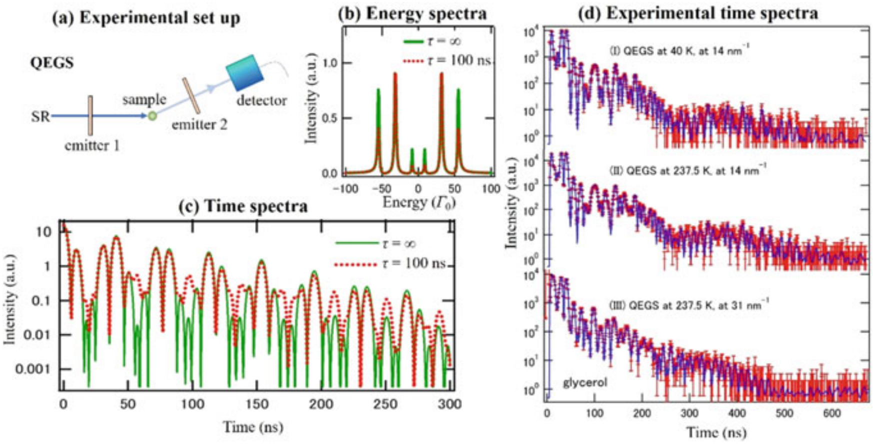

Fig. 2.22 **a** Experimental setup, **b** theoretical energy spectra and **c** theoretical time spectra, and **d** experimentally obtained time spectra from QEGS studies on glycerol. The spectra were obtained (I) at 40 K at 14 nm^{-1}, (II) at 237.5 K at 14 nm^{-1}, and at 237.5 K at 31 nm^{-1}. In panel **d**, the points and vertical bars represent experimentally obtained counts of γ-rays and statistic errors (standard deviations), respectively. The lines represent fitting curves using eq. (2.23)

2.4.6 Results Obtained by Quasielastic Scattering Experiment Using Time-Domain Interferometry of Mössbauer Gamma Rays

So far, QEGS measurements using TDI were performed for alloys, liquid crystals, molecular liquids, ionic liquids, super-ionic conducting glasses, polymers, and polymer nanocomposites. For supercooled glass formers, van der Waals molecular liquid *o*-terphenyl, hydrogen bonding liquid glycerol, ionic liquids, and polymer polybutadiene were measured to study the microscopic dynamics toward glass transition. In glycerol and polybutadiene, the so-called de Gennes narrowing was observed by the q-dependent studies of the structural relaxation process called as the α-process [128]. In addition to the α-process, a local activation process called as the Johari-Goldstein (JG) β-process was observed in *o*-terphenyl and polybutadiene [124, 128]. The branching temperature of the JG β-process from the α-process, which could not be determined by conventional methods, such as dielectric spectroscopy, was accurately obtained. The study of ionic liquid 1-butyl-3-methylimidazolium iodide revealed that the ionic liquids are classified as so-called fragile glass formers [125]. For superionic conducting Na_3PS_4 glass, it was revealed that angstrom-scale translational motion of a part of Na ions occurs at picosecond to nanosecond time scale, while the movement of PS_4 ions rarely occur [129].

To understand the microscopic origin of the shear viscosity, a higher alcohol 3,7-dimethyl-1-octanol with nanometric domain structures was studied using the multiline TDI system [130]. The dynamics of both nanometric- and molecular-scale structures were found to relate to the slower and faster relaxation modes of the shear viscosity. The effect of the presence of Si nanoparticles on bulk polymer (polybutadiene) dynamics was studied for a polymer nanocomposite system [131]. B2 alloy CoGa was studied using the single-line TDI, and the possibility of the atomic diffusion study using diffuse scattering was shown [132].

For soft materials, QEGS was applied for dynamics study of liquid crystal molecules 4-cyano-4’-octylbiphenyl and 11-(4’-cyanobiphenyl-4-yloxy) undecyl pentadecafluorooctanoate under layered structure in the smectic phase [133]. Both the interlayer and intralayer molecular relaxation times were successfully observed using the multiline TDI system. The layer order parameter of the smectic phase was determined, and the anomalous diffusion coefficient could be obtained using the multiline TDI system [134]. The study of cholesteric blue phase revealed that the emergence of the mesostructure is irrelevant to the microscopic molecular structure and dynamics in this system [135]. TDI allows the study of molecular dynamics in smectic, nematic, and cholesteric phases.

2.4.7 *Summary and Perspective of Quasielastic Scattering of Mössbauer Gamma Rays*

Quasielastic scattering technique using SR-based Mössbauer γ-rays is a promising technique to directly reveal the microscopic dynamics in unique timescales between nanosecond and microsecond.

The quasielastic scattering technique using TDI will be improved by further developments, such as an increase in detection detector efficiency, an increase in the solid angle of γ-ray detection by introducing more detectors, and an increase in γ-ray count rate using more γ-ray lines for measurement. These improvements greatly help in extracting the intermediate scattering function from the spectrum and directly visualizing the decay of the intermediate scattering function.

QEGS using ^{57}Fe nuclear Bragg monochromator is expected to measure the dynamics faster than the timescale covered by current QEGS using TDI, for example, up to 100 ps. Therefore, the development of the energy-domain QEGS system and the combination study with the TDI system expand the accessible timescales by QEGS using the Mössbauer γ-rays. In addition, a further combination study with other techniques, such as quasielastic neutron scattering, allows us to further understand microscopic dynamics in complex systems. These improvements and combination studies are important to understand the macroscopic properties and functions from a microscopic level for both basic science and industrial applications. Furthermore, the TDI system can be applied for studies on dynamical correlations in quantum systems [136].

The fourth-generation SR shows much higher spatial coherency and higher condensing properties than the third-generation SR used for the studies introduced here. Microscopic dynamics of each spatial region in complex systems can be measured selectively by focusing on the γ-rays. Such QEGS system with focused γ-rays is useful, for example, to understand dynamical heterogeneity of glass formers.

Acknowledgements The author is grateful to all collaborators and would like to thank all of the staff at the Institute for Integrated Radiation and Nuclear Science, Kyoto University, National Institutes for Quantum and Radiological Science and Technology, Japan Atomic Energy Agency, SPring-8, and the Photon factory of KEK for their support.

References

1. For example, N.N. Greenwood, T.C. Gibb, *Mössbauer Spectroscopy.* (Chapman and Hall, London, 1971)
2. D.C. Champeney, Rep. Prog. Phys. **42**, 1017 (1979). and references therein
3. Please see Chap. 1 in this book
4. M. Seto, S. Kitao, Y. Kobayashi, R. Haruki, T. Mitsui, Y. Yoda, X.W. Zhang, Yu. Maeda, Phys. Rev. Lett. **84**, 566 (2000)
5. M. Seto, Y. Yoda, S. Kikuta, X.W. Zhang, M. Ando, Phys. Rev. Lett. **74**, 3828 (1995)

6. M. Seto, S. Kitao, Y. Kobayashi, R. Haruki, Y. Yoda, T. Mitsui, T. Ishikawa, Phys. Rev. Lett. **91**, 185505 (2003)
7. M. Seto, R. Masuda, S. Higashitaniguchi, S. Kitao, Y. Kobayashi, C. Inaba, T. Mitsui, Y. Yoda, Phys. Rev. Lett. **102**, 217602 (2009)
8. R. Masuda, Y. Kobayashi, S. Kitao, M. Kurokuzu, M. Saito, Y. Yoda, T. Mitsui, F. Iga, M. Seto, Appl. Phys. Lett. **104**, 082411 (2014)
9. Mössbauer Spectroscopy Periodic Table and Isotopes, Mössbauer Effect Data Center, Dalian, China. http://www.medc.dicp.ac.cn/Resources.php. Accessed 30 Apr 2019
10. D.W. Hafemeister, Phys. Rev. Lett. **14**, 593 (1965)
11. M. Seto, J. Phys. Soc. Jpn. **82**, 021016 (2013)
12. S.L. Ruby, J. Phys. (Paris), Colloq. **35**, C6-209 (1974)
13. E. Gerdau, R. Rüffer, H. Winkler, W. Tolksdorf, C.P. Klages, J.P. Hannon, Phys. Rev. Lett. **54**, 835 (1985)
14. J.B. Hastings, D.P. Siddons, U. van Brück, R. Hollatz, U. Bergmann, Phys. Rev. Lett. **66**, 770 (1991)
15. T. Shinjo, M. Kiyama, K. Sugita, K. Watanabe, T. Takada, J. Magn. Magn. Mater. **35**, 133 (1983)
16. T. Mitsui, R. Masuda, M. Seto, E. Suharyadi, K. Mibu, J. Synchrotron Radiat. **19**, 198 (2011)
17. T. Nakano, N. Fukuda, M. Seto, Y. Kobayashi, R. Masuda, Y. Yoda, M. Mihara, Y. Nozoe, Phys. Rev. B **91**, 140101(R) (2015)
18. S. Kishimoto, F. Nishikido, R. Haruki, K. Shibuya, M. Koshimizu, Hyperfine Interact. **204**, 101 (2012)
19. K. Mibu, M. Seto, T. Mitsui, Y. Yoda, R. Masuda, S. Kitao, Y. Kobayashi, E. Suharyadi, M. Tanaka, M. Tsunoda, H. Yanagihara, E. Kita, Hyperfine Interact. **217**, 127 (2013)
20. M. Kurokuzu, S. Kitao, Y. Kobayashi, M. Saito, R. Masuda, T. Mitsui, Y. Yoda, M. Seto, Hyperfine Interact. **226**, 687 (2014)
21. S. Tsutsui, R. Masuda, Y. Kobayahi Yoda, K. Mizuuchi, Y. Shimizu, H. Hidaka, T. Yanagisawa, H. Amitsuka, F. Iga, M. Seto, J. Phys. Soc. Jpn. **85**, 083704 (2016)
22. M. Seto, R. Masuda, S.S. Higashitaniguchi Kitao, Y. Kobayashi, C. Inaba, T. Mitsui, Y. Yoda, J. Phys: Conf. Ser. **217**, 012002 (2010)
23. J. Yamaura, H. Ohsumi, K. Sugimoto, S. Tsutsui, Y. Yoda, S. Takeshita, A. Tokuda, S. Kitao, M. Kurokuzu, M. Seto, I. Yamauchi, K. Ohgushi, M. Takigawa, T. Arima, Z. Hiroi, J. Phys: Conf. Ser. **391**, 012112 (2012)
24. S. Kishimoto, Nucl. Inst. Meth. Phys. Res. A **309**, 603 (1991)
25. T. Matsuoka, H. Fujihisa, N. Hirao, Y. Ohishi, T. Mitsui, R. Masuda, M. Seto, Y. Yoda, K. Shimizu, A. Machida, K. Aoki, Phys. Rev. Lett. **107**, 025501 (2011)
26. G.V. Smirnov, U. van Brück, J. Arther, G.S. Brown, A.I. Chumakov, A.Q.R. Baron, W. Petry, S.L. Ruby, Phys. Rev. A. **76** (2007)
27. F.J. Lynch, R.E. Holland, M. Hamermesh, Phys. Rev. **120**, 513 (1960)
28. D.W. Hamill, G.R. Hoy, Phys. Rev. Lett. **21**, 724 (1968)
29. R.B. Firestone, V.S. Shirley (eds.), *Table of Isotopes*, 8th edn. (Willey, New York, 1996)
30. E.A. McCutchan, Evaluated nuclear structure data file search and retrieval, Last updated 2019-03-15. National Nuclear Data Center, Brookhaven National Laboratory, New York. (2019) https://www.nndc.bnl.gov/ensdf/ensdf.jsp. Accessed 30 Apr 2019
31. S. Sasaki, KEK report **90–16** (1990) 1–-143. This report is also in database form at http://www.sasakiken.net/abcoeff/abcoeff2.html
32. M.J. Berger, J.H. Hubbell, S.M. Seltzer, J. Chang, J.S. Coursey, R. Sukumar, D.S. Zucker, K. Olsen, XCOM: photon cross sections database (version 1.5), NIST Standard Reference Database 8 (XGAM), Online Mar 1998 – Last Update Nov 2010. National Institute of Standards and Technology, Maryland, (2010) http://physics.nist.gov/xcom. Accessed in 30 Apr 2019
33. M.J. Berger, J.H. Hubbell, NBSIR **87–3597**, 1 (1987)
34. M.J. Berger, J.H. Hubbell, NIST x-ray and gamma-ray attenuation coefficients and cross sections database. NIST Standard Reference Database 8, Version 2.0, National Institute of Standards and Technology, Gaithersburg, MD, (1990)

35. K. Kanaya, S. Okayama, J. Phys. D Appl. Phys. **5**, 43 (1972)
36. ESTAR (1984) National Institute of Standards and Technology, Maryland, USA. https://physics.nist.gov/PhysRefData/Star/Text/ESTAR.html. Accessed 30 Apr 2019
37. M.J. Berger, M. Inokuti, H.H. Anderson, H. Bichsel, J.A. Dennis, D. Powers, S.M. Seltzer, J.E. Turner, J. Int. Comm. Radiat. Units Meas. os19 (1984) Report 37
38. G.K. Shenoy, F.E. Wagner (eds.), *Mössbauer Isomer shifts* (North-Holland, Amsterdam, 1978)
39. P. Gütlich, E. Bill, A.X. Trautwein, *Mössbauer spectroscopy and transition metal chemistry: fundamentals and applications* (Springer, Berlin, 2011)
40. G.V. Smirnov, V.V. Sklyarevskii, R.A. Voskanyan, A.N. Artem'ev, JETP Lett. **9**, 70 (1969)
41. W. Sturhahn, T.S. Toellner, E.E. Alp, X. Zhang, M. Ando, Y. Yoda, S. Kikuta, M. Seto, C.W. Kimball, B. Dabrowski, Phys. Rev. Lett. **74**, 3832 (1995)
42. A.I. Chumakov, R. Rüffer, H. Grünsteudel, H.F. Grünsteudel, G. Grübel, J. Metge, O. Leupold, H.A. Goodwin, Europhys. Lett. **30**, 427 (1995)
43. M. Yabashi, K. Tamasaku, S. Kikuta, T. Ishikawa, Rev. Sci. Instrum. **72**, 4080 (2001)
44. H.C. Wille, R.P. Hermann, I. Sergueev, O. Leupold, P. Van der Linden, B.C. Sales, F. Grandjean, G.J. Long, R. Rüffer, V. Shvyd'ko Yu, Phys. Rev. B **76**, 140301(R) (2007)
45. Yu.V. Shvyd'ko, *X-Ray Optics*, Springer Series in Optical Sciences **98**, (Berlin, Springer, 2004)
46. K.S. Singwi, A. Sjölander, Phys. Rev. **120**, 1093 (1960)
47. V.G. Kohn, A.I. Chumakov, R. Rüffer, Phys. Rev. B **58**, 8437 (1998)
48. V.G. Kohn, A.I. Chumakov, Hyperfine Interact. **125**, 205 (2000)
49. J. Matsuno, M. Seto, S. Kitao, Y. Kobayashi, R. Haruki, T. Mitsui, A. Fujimoril, Y. Takeda, S. Kawasaki, M. Takano, J. Phys. Soc. Jpn. **73**, 2768 (2004)
50. S. Higashitaniguchi, M. Seto, S. Kitao, Y. Kobayashi, M. Saito, R. Masuda, T. Mitsui, Y.Y. Yoda Kamihara, M. Hirano, H. Hosono, Phys. Rev. B **78**, 174507 (2008)
51. M. Seto, Y. Kobayashi, S. Kitao, R. Haruki, T. Mitsui, Y. Yoda, S. Nasu, S. Kikuta, Phys. Rev. B **61**, 11420 (2000)
52. G. Gila, R.M. Nicklow, Phys. Rev. **143**, 487 (1966)
53. P.D. Mannheim, Phys. Rev. **165**, 1011 (1968)
54. C. Keppler, K. Achterhold, A. Ostermann, U. Van Bürck, W. Potzel, A.I. Chumakov, A.Q.R. Baron, R. Rüffer, F. Parak, European. Biophys. J. **25**, 221 (1997)
55. F. Parak, K. Achterhold, Hyperfine Interact. **123/124** Part I, 825 (1999)
56. J.T.S. Sage, M. Durbin, W. Sturhahn, D.C. Wharton, P.M. Champion, P. Hession, J. Sutter, E.E. Alp, Phys. Rev. Lett. **86**, 4966 (2001)
57. J.T. Sage, C. Paxson, G.R.A. Wyllie, W. Sturhahn, S. Durbin M, P.M. champion, E.E. Alp, W.R. Scheidt, J. Phys.: Condens. Matter **13**, 7707 (2001)
58. Y. Xiao, H. Wang, S.J. George, M.C. Smith, M.W. Adams, F.E. Jenney Jr., W. Sturhahn, E.E. Alp, J. Zhao, Y. Yoda, A. Dey, E.I. Solomon, S.P. Cramer, J. Am. Chem. Soc. **127**, 14596 (2005)
59. T. Petrenko, S.D. George, N. Aliaga-Alcalde, E. Bill, B. Mienert, Y. Xiao, Y. Guo, W. Sturhahn, S.P. Cramer, K. Wieghardt, F. Neese, J. Am. Chem. Soc. **129**, 11053 (2007)
60. S.J. George, R.Y. Igarashi, Y. Xiao, J.A. Hernandez, M. Demuez, D. Zhao, Y. Yoda, P.W. Ludden, L.M. Rubio, S.P. Cramer, J. Am. Chem. **130**, 5673 (2008)
61. C.B. Bell III, S.D. Wong, Y. Xiao, E.J. Klinker, A.L. Tenderholt, M.C. Smith, J.U. Rohde, L. Que Jr., S.P. Cramer, E.I. Solomon, Angew. Chem. Int. Ed. **47**, 9071 (2008)
62. F. Paulat, T.C. Berto, S.D. George, L. Goodrich, V.K. Praneeth, C.D. Sulok, N. Lehnert, Inorg. Chem. **47**, 11449 (2008)
63. W. Zeng, N.J. Silvernail, W.R. Scheidt, J.T. Sage, Nuclear Resonance Vibrational Spectroscopy (NRVS), *Encyclopedia of Inorganic Chemistry* (2008)
64. W.R. Scheidt, A. Barabanschikov, J.W. Pavlik, N.J. Silvernail, J.T. Sage, Inorg. Chem. **49**, 6240 (2010)
65. Z.J. Tonzetich, H. Wang, D. Mitra, C.E. Tinberg, L.H. Do, F.E. Jenney, M.W.W. Adams, S.P. Cramer, S.J. Lippard, J. Am. Chem. Soc. **132**, 6914 (2010)

66. C.E. Tinberg, Z.J. Tonzetich, H. Wang, L.H. Do, Y. Yoda, S.P. Cramer, S.J. Lippard, J. Am. Chem. Soc. **132**, 18168 (2010)
67. W. Zeng, N.J. Silvernail, W.R. Scheidt, J.T. Sage, Nuclear Resonance Vibrational Spectroscopy (NRVS). In *Encyclopedia of Inorganic Chemistry*, 2008 (published online)
68. S. Kamali, H. Wang, D. Mitra, H. Ogata, W. Lubitz, B.C. Manor, T.B. Rauchfuss, D. Byrne, V. Bonnefoy, F.E. Jenney Jr, M.W. Adams, Y. Yoda, E. Alp, J. Zhao, S.P. Cramer, Angew. Chem. Int. Ed. **52**, 724 (2013)
69. D. Mitra, S.J. George, Y. Guo, S.S. Kamali Keable, J.W. Peters, V. Pelmenschikov, D.A. Case, S.P. Cramer, J. Am. Chem. Soc. **135**, 2530 (2013)
70. T. Ohta, J.G. Liu, M. Saito, Y. Kobayashi, Y. Yoda, M. Seto, Y. Naruta. J. Phys. Chem. B **116**, 13831 (2012)
71. K. Park, C.B. Bell III, L.V. Liu, D. Wang, G. Xue, K. Kwak, S.D. Wong, K.M. Light, J. Zhao, E.E. Alp, Y. Yoda, M. Saito, Y. Kobayashi, T. Ohta, M. Seto, L. Que Jr., E.I. Solomon, Proc. Natl. Acad. Sci. U.S.A. **110**, 6275 (2013)
72. S.D. Wong et al., Nature **499**, 320 (2013)
73. H. Ogata et al., Nat. Commun. **6**, 7890 (2015)
74. K. Sutherlin et al., J. Am. Chem. Soc. **138**, 14294 (2016)
75. E.J. Reijerse et al., J. Am. Chem. Soc. **139**, 4306 (2017)
76. V. Pelmenschikov et al., J. Am. Chem. Soc. **139**, 16894 (2017)
77. R. Lübbers, H.F. Grünsteudel, A.I. Chumakov, G. Wortmann, Science **287**, 1250 (2000)
78. H.K. Mao, J. Xu, V.V. Struzhkin, J. Shu, R.J. Hemley, W. Sturhahn, M.Y. Hu, E.E. Alp, L. Vocadlo, D. Alfè, G.D. Price, M.J. Gillan, M. Schwoerer-Böhning, D. Häusermann, P. Eng, G. Shen, H. Giefers, R. Lübbers, G. Wortmann, Science **292**, 914 (2001)
79. J.F. Lin, W. Sturhahn, J. Zhao, G. Shen, H.K. Mao, R.J. Hemley, Science **308**, 1892 (2005)
80. B. Fultz B, C.C. Ahn, E.E. Alp, W. Sturhahn, T.S. Toellner, Phys. Rev. Lett., **79**, 937 (1997)
81. L. Pasquini, A. Barla, A.I. Chumakov, O. Leupold, R. Rüffer, A. Deriu, E. Bonetti, Phys. Rev. B **66**, 73410 (2002)
82. S. Stankov, Y.Z. Yue, M. Miglierini, B. Sepiol, I. Sergueev, A.I. Chumakov, L. Hu, P. Svec, R. Rüffer, Phys. Rev. Lett. **100**, 235503 (2008)
83. Y. Tamada, R. Masuda, A. Togo, S. Yamamoto, Y. Yoda, I. Tanaka, M. Seto, S. Nasu, T. Ono, Phys. Rev. B **81**, 132302 (2010)
84. S. Couet, M. Sternik, B. Laenens, A. Siegel, K. Parlinski, N. Planckaert, F. Gröstlinger, A.I. Chumakov, R. Rüffer, B. Sepiol, K. Temst, A. Vantomme, Phys. Rev. B **82**, 094109 (2010)
85. S. Stankov, M. Miglierini, A.I. Chumakov, I. Sergueev, Y.Z. Yue, B. Sepiol, P. Svec, L. Hu, R. Rüffer, Phys. Rev. B **82**, 144301 (2010)
86. W. Keune, W. Sturhahn, Hyperfine Interact., **123/124** Part I, 847 (1999)
87. R. Röhlsberger, W. Sturhahn, T.S. Toellner, K.W. Quast, E.E. Alp, A. Bernhard, J. Metge, R. Rüffer, E. Burkel, Phys. B **263–264**, 581 (1999)
88. W. Sturhahn, R. Röhlsberger, E.E. Alp, T.T. Ruckert Schrör, W. Keune, J. Magn. Magn. Mater. **198–199**, 590 (1999)
89. T. Ruckert, W. Keune, W. Sturhahn, M.Y. Hu, J.P. Sutter, T.S. Toellner, E.E. Alp, Hyperfine Interact. **126**, 363 (2000)
90. B.R. Cuenya, W. Keune, W. Sturhahn, T.S. Toellner, M.Y. Hu, Phys. Rev. B **64**, 235321 (2001)
91. S. Couet, K. Schlage, R. Rüffer, S. Stankov, Th Diederich, B. Laenens, R. Röhlsberger, Phys. Rev. Lett. **103**, 097201 (2009)
92. S. Stankov, R. Röhlsberger, T. Ślęzak, M. Sladecek, B. Sepiol, G. Vogl, A.I. Chumakov, R. Rüffer, N. Spiridis, J. Łażewski, K. Parliński, J. Korecki, Phys. Rev. Lett. **99**, 185501 (2007)
93. R.A. Brand, G. Coddens, A.I. Chumakov, Y. Calvayrac, Phys. Rev. B **59**, 14145 (1999)
94. R.P. Hermann, W. Schweika, O. Leupold, R. Rüffer, G.S. Nolas, F. Grandjean, G.J. Long, Phys. Rev. B **71**, 174301 (2005)
95. J.S. Tse, D.D. Klug, J.Y. Zhao, W. Sturhahn, E.E. Alp, J. Baumert, C. Gutt, M.R. Johnson, W. Press, Nat. Mater. **4**, 917 (2005)

96. V. Ksenofontov, G. Wortmann, A.I. Chumakov, T. Gasi, S. Medvedev, T.M. McQueen, R.J. Cava, C. Felser, Phys. Rev. B **81**, 184510 (2010)
97. S. Tsutsui, C.H. Lee, C. Tassel, Y. Yoshida, Y. Yoda, K. Kihou, A. Iyo, H. Eisaki, J. Phys. Soc. Jpn. **79**, 013706 (2010)
98. H. Kobayashi, S. Ikeda, Y. Yoda, H. Nakamura, Machida: M Phys. Rev. B **84**, 184304 (2011)
99. G.J. Long, R.P. Hermann, F. Grandjean, E.E. Alp, W. Sturhahn, C.E. Johnson, D.E. Brown, O. Leupold, R. Rüffer, Phys. Rev. B **71**, 140302 (2005) (R)
100. S. Tsutsui, H. Kobayashi, D. Ishikawa, J.P. Sutter, A.Q.R. Baron, T. Hasegawa, N. Ogita, M. Udagawa, Y. Yoda, H. Onodera, D. Kikuchi, H. Sugawara, C. Sekine, I. Shirotani, H. Sato, J. Phys. Soc. Jpn. **77**, 033601 (2008)
101. A.I. Chumakov, G. Monaco, A. Monaco, W.A. Crichton, A. Bosak, R. Rüffer, A. Meyer, F. Kargl, L. Comez, D. Fioretto, H. Giefers, S. Roitsch, G. Wortmann, M.H. Manghnani, A. Hushur, Q. Williams, J. Balogh, K. Parliński, P. Jochym, P. Piekarz, Phys. Rev. Lett. **106**, 225501 (2011)
102. A.I. Chumakov, Hyperfine Interact. **207**, 107 (2012)
103. X.W. Zhang, Y. Yoda, M. Seto, Yu. Maeda, M. Ando, S. Kikuta, Jpn. J. Appl. Phys. **34**, L330 (1995)
104. R. Haruki, M. Seto, S. Kitao, Y. Yoda, Maeda Yu. J. Phys. Soc. Jpn. **69**, 4049 (2000)
105. R. Haruki, M. Seto, S. Kitao, Y. Kobayashi, Y. Yoda, T. Mitsui, Maeda Yu. J. Phys. Soc. Jpn. **70**, 445 (2001)
106. For a review, see N. Tsuda, K. Nasu, A. Fujimori, K. Shiratori, *Electronic Conduction in Oxide*s, 2nd edn. (Springer-Verlag, Berlin, 2000), M. Imada, A. Fujimori, Y. Tokura, Rev. Mod. Phys. **70**, 1039, Sec. E (1998)
107. M. Takano, N. Nakanishi, Y. Takeda, S. Naka, T. Takada, Mater. Res. Bull. **12**, 923 (1977), M. Takano, J. Kawachi, N. Nakanishi, Y. Takeda, J. Solid State Chem. **39**, 75 (1981)
108. For a review, see P. Gutlich: in "*M*össbauer *Spectroscopy Applied to Inorganic Chemistry"* vol 1, ed. by G.J. Long (Plenum, New York, 1984) pp. 287–337
109. T. Ishikawa, H. Nakazaki, A. Yasukawa, K. Kandori, M. Seto, Mater. Res. Bull. **33**, 1609 (1998)
110. J.A. Elliott, H.E. Hall, Bunbury D St P: Proc. Phys. Soc. **89**, 595 (1966)
111. D.C. Champeney, W.D. Woodhams, J. Phys. B **1**, 620 (1968)
112. R. Röhlsberger, *Nuclear Condensed Matter Physics with Synchrotron Radiation* (Springer-Verlag, Berlin, 2005)
113. J.Z. Tischler, B.C. Larson, L.A. Boatner, E.E. Alp, T. Mooney, J. Appl. Phys. **79**, 3686 (1996)
114. R. Masuda, T. Mitsui, Y. Kobayashi, S. Higashitaniguchi, M. Seto, Jpn. J. Appl. Phys. **48**, 120221 (2009)
115. A.Q.R. Baron et. al., Phys. Rev. Lett. **79**, 2823 (1997)
116. T. Ishikawa et. al., Rev. Sci. Instrum. **63**, 1015 (1992)
117. G.V. Smirov, Hyperfine Interact. **123**(124), 31 (1999)
118. Yu. Kagan, A.M. Afanas'ev, V.G. Kohn, Phys. C **12**, 615 (1979)
119. G.V. Smirnov, V.G. Kohn, W. Petry, Phys. Rev. B **63**, 144303 (2001)
120. G.T. Tramell, Phys. Rev. Lett. **126**, 1045 (1962)
121. M. Saito, R. Masuda, Y. Yoda, M. Seto, Sci. Rep. **7**, 12558 (2017)
122. G.V. Smirnov et. al., Phys. Rev. B **73**, 184126 (2006)
123. U. Balucani, M. Zoppi, *Dynamics of the Liquid State* (Oxford University Press, UK, 1994)
124. M. Saito et. al., Phys. Rev. Lett. **109**, 115705 (2012)
125. M. Saito et. al., Appl. Phys. Express **2**, 026502 (2009)
126. M. Saito et. al., Hyperfine Interact. **206**, 87 (2012)
127. F. Caporaletti et. al., Rev. Sci. Instrum. **88**, 105114 (2017)
128. T. Kanaya, R. Inoue, M. Saito, M. Seto, Y. Yoda, J. Chem. Phys. **140**, 144906 (2014)
129. M. Saito et. al., Phys. Status Solidi B **257**, 2000113 (2020)
130. T. Yamaguchi et. al., J. Phys. Chem. Lett. **9**, 298 (2018)
131. M. Saito et al., Hyperfine Interact. **238**, 99 (2017)
132. M. Kaisermayr et. al., Eur. Phys. J. B **20**, 335 (2001)

133. M. Saito et. al., J. Phys. Soc. Jpn. **81**, 023001 (2012)
134. M. Saito et. al., Phys. Rev. Res. **1**, 012008(R) (2019)
135. M. Saito et. al., Hyperfine Interact. **241**, 14 (2020)
136. S. Castrignano, J. Evers, Phys. Rev. Lett. **122**, 025301 (2019)